Roles of microstructure in fatigue crack initiation

Kwai S. Chan *

Southwest Research Institute, 6220 Culebra Road, San Antonio, TX 78238, United States

ARTICLE INFO

ABSTRACT

Fatigue failure in the high-cycle and ultrahigh-cycle regimes is often dominated by the crack initiation processes, which are strongly influenced by the salient features and defects in the microstructure. Competing fatigue mechanisms involving crack initiation at persistent slipbands, grain boundaries, pores, and non-metallic inclusions or particles, have been reported to occur at surface sites in the high-cycle fatigue regime (10^6–10^7 cycles), but shift to interior sites in the ultrahigh-cycle fatigue regime (10^9–10^{10} cycles). The changes in fatigue mechanism and crack initiation site result in large variations in fatigue life. This overview article examines the roles of microstructural features such as grain size, texture, porosity, non-metallic inclusion in the fatigue crack initiation process and the manners by which these microstructural effects affect the shape of the stress–life curves.

© 2009 Elsevier Ltd. All rights reserved.

1. Introduction

Crack initiation is a term used differently by scientists studying fatigue in the laboratory and engineers designing and maintaining structures. To the scientist, initiation is the number of cycles required to generate, nucleate, or form the smallest crack that they can detect by any means [1]. In more recent literature, crack incubation and crack formation are also used interchangeably to describe this process. On this basis, initiation sets the limit on the minimum size of a small fatigue crack [2], assuming that the component does not have any existing cracks. Typically, initiation is a complex process that can lead to a crack that is extremely small (<1 μm) or one that "pops in" (initiates and rapidly grows) at up to 100 μm long. To the engineer, initiation is likely to mean the smallest crack or an engineering-sized crack that can be determined by a reliable non-destructive evaluation (NDE) technique, which would, to the scientist, probably mean that the growth of small cracks is included in this definition. In this paper, the scientific definition of crack initiation is adapted and the term is taken to mean the process of forming a fatigue crack of a length that is on the order of a grain size or less.

A fatigue crack is formed as the result of localized plastic deformation during cyclic straining [3–8]. The nature of the slip characteristics often dictates the surface topography near the crack initiation site and the fatigue crack initiation process. In pure metals and some alloys without pores or inclusions, irreversible dislocation glides under cyclic loading leading to the development of persistent slipbands (PSBs), extrusions, and intrusions in surface grains [3–8] that are optimally oriented for slip [3–9]. With continued strain cycling, a fatigue crack can develop at an extrusion or intrusion within a persistent slipband. The processes responsible for the formation of persistent slipbands, extrusions, and fatigue cracks in surface grains are well established, as described in several reviews [3–8]. Fatigue cracks initiated by the intrusion–extrusion mechanism from persistent slipbands are referred to as Stage I cracks, which form on the active slip plane that lies at an angle (e.g., 45°) to the stress axis. As the slipband or Stage I cracks grow larger, they alter the crack path to grow more perpendicular to the stress axis, eventually becoming Stage II fatigue cracks [4–6].

In commercial materials, fatigue cracks often start at metallurgical stress concentrations such as inclusions and pores. The crystallographic anisotropy, i.e., texture, of a material also has strong influences. In some alloys, fatigue cracks nucleate within a local region where a number of adjacent grains of nearly the same orientation have the slip characteristics of a single large grain. Cracks can also initiate in grain boundaries, with or without the influence of environment, or at grain boundary brittle intermetallics, or due to the chemical segregation of impurities to the grain boundary [10]. Surface finish has a strong influence on fatigue crack initiation [11] and residual stresses due to surface preparation can have considerable influence on the number of cycles to initiation.

The complex microstructures in structural metals and engineering alloys result in a number of features that are potential sites where competing fatigue crack initiation mechanisms may occur. As an example, fatigue crack formation in Ni-based superalloys

* Tel.: +1 210 522 2053; fax: +1 210 522 6965.
E-mail address: kchan@swri.edu

can occur at planar slipbands, grain boundaries, pores, and inclusions, depending on processing condition, temperature, stress or strain range, loading frequency, and environment [12]. A number of recent reports have identified substantial fatigue life variations in structural alloys that exhibit multiple competing crack initiation mechanisms [13–15]. While the worst-case fatigue life regime is often dominated by the growth of small cracks [15], crack initiation at multiple sites is usually involved.

The complexity of the fatigue crack initiation processes is most evident in the ultrahigh-cycle fatigue (UHCF) regime [16–18], where the cycle to failure exceeds 10^9 cycles. Extensive experimental studies indicated conventional fatigue limit defined as run-out at 10^7 cycles (HCF) is not a "true" endurance limit in many metals and alloys, which may show failure when the number of fatigue cycles is extended into the UHCF regime. Two types of S–N_f curves have been proposed for UHCF, which are illustrated in Fig. 1a and b [16–18]. The S–N_f curve in Fig. 1a exhibits two dual fatigue limits, an apparent one in the 10^6–10^7 cycles and a lower limit in the 10^9–10^{10} cycles. The transition is accompanied by a change in the fatigue crack initiation mechanism from crystallographic surface facets to pores and inclusions in interior grains. The S–N_f curve shown in Fig. 1b manifests one apparent fatigue limit in the 10^6–10^7 cycles but the stress amplitude decreases further with increasing fatigue cycles in the 10^9–10^{10} cycles without the presence of an endurance limit. In a recent paper, Mughrabi [18]

suggested that multiple fatigue limits, each corresponding to individual crack initiation mechanisms, can exist in an S–N_f curve.

The objective of this article to assess the role of various constituents of the microstructure in the fatigue crack initiation processes including those at slipbands, pores, grain boundaries, and inclusions. Particular attention is focused on identifying pertinent microstructural or micromechanical parameters for the various crack initiation mechanisms operative in surface grains or in interior grains. Relevant parameters are utilized to elucidate scenarios that can lead to the transition of surface crack initiation to subsurface initiation and the formation of double fatigue limits in some alloys and their absence in others. In this article, crack initiation at slipbands and grain boundaries is considered in Section 2. Fatigue crack initiation at pores and inclusions is treated in Sections 3 and 4, respectively. The process of fatigue crack initiation from machined surfaces is described in Section 5, which is then followed by prospects and challenges for future development in Section 6 and concluding remarks in Section 7.

## 2. Fatigue crack initiation at slipbands

2.1. Persistent slipbands

In pure metals and some alloys, irreversible dislocation glides under cyclic loading lead to the development of persistent slipbands (PSBs), extrusions, and intrusions in surface grains that are optimally oriented for slip. The evolution of dislocation structures as a function of strain amplitude and cyclic stress–strain behaviors has been investigated for a number of metals and alloys, mostly notably Cu [4–6], Ni [19–22], Ti [23], and steels [23–26]. The processes responsible for the formation of persistent slipbands, extrusions, and fatigue cracks in surface grains are well established, as described in several reviews [4–6]. In general, planar slip is prevalent in materials with a low stacking fault, while wavy slip is more prevalent in materials with high stacking fault energy [27].

Recent works on surface crack initiation have focused on the evolution of slip morphology with fatigue cycles. Harvey et al. [23] reported the first atomic force microscopy (AFM) measurements of slip spacing and slip height displacement for fatigue of Ti and HSLA steel. Using atomic force microscopy and high-resolution scanning electron microscopy, Polak and coworkers [24–26] showed that the surface roughness in two cyclically loaded stainless steels was caused by persistent slip marking formed by extrusions and intrusions. Their results showed that the mean extrusion height appeared to increase linearly with fatigue cycles in a 316 stainless steel, but non-linearly in a ferritic stainless steel. A dislocation dynamics model has been utilized to simulate the evolution of dislocation structures in 316L austenitic stainless steels for single slip and multiple slip conditions [28]. The results indicated that cross slip is responsible for redistributing slip among slipbands.

Chan et al. [29] recently studied the evolution of slip morphology in the surface grains of Ni200 during low-cycle fatigue by measuring the slipband width (h) and spacing (w), which are defined in Fig. 2a. They showed that in Ni200, the slipband width, the slipband spacing, and the slipband-width-to-spacing ratio all varied with fatigue cycles and show substantial variations among individual grains. The slip morphology of Ni200 is illustrated in Fig. 2b. The slipband width (h), spacing (w), and the width-to-spacing ratio were correlated as a function of the number of fatigue cycle, N, in a double logarithm plot. There appears to be a linear relation between log (h/w) ratio and log N with a slope of 0.168, Fig. 2c. The increase of the h/w ratio was the result of an increase of the slipband width (h) and a decrease of the slipband spacing (w) with increasing fatigue cycles.

Chan et al. [29] also measured the local slipband morphologies in Ni200 specimens near the onset of fatigue fracture. The h/w ra-
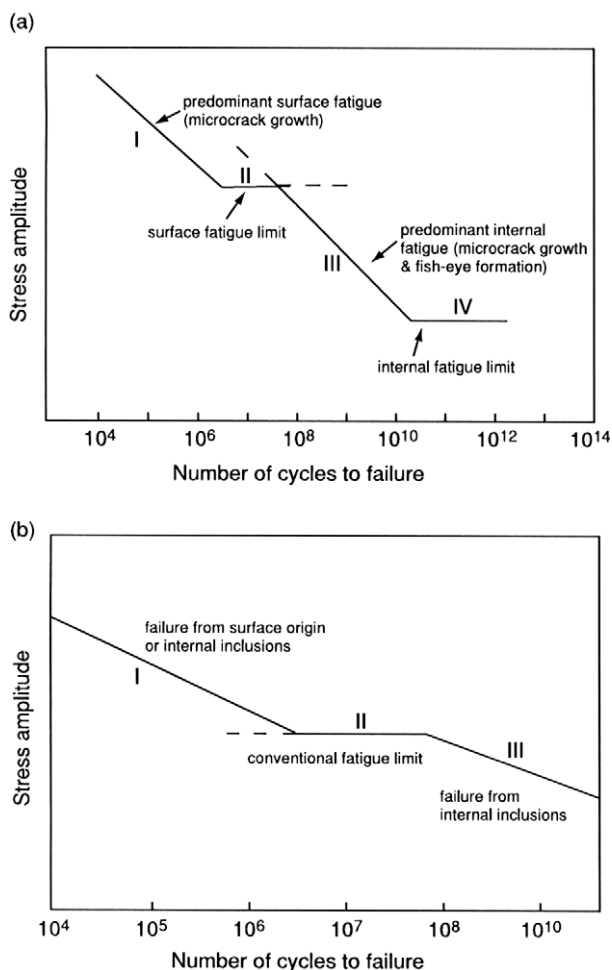

Fig. 1. Schematics of multi-stage stress–life (S–N_f) curves: (a) S–N_f curve with double fatigue limits for surface and internal initiation, and (b) S–N_f curve with an apparent fatigue limit for surface initiation but without one for interior initiation. From Nishijima and Kanazawa [16], Murakami et al. [17], and Mughrabi [18].
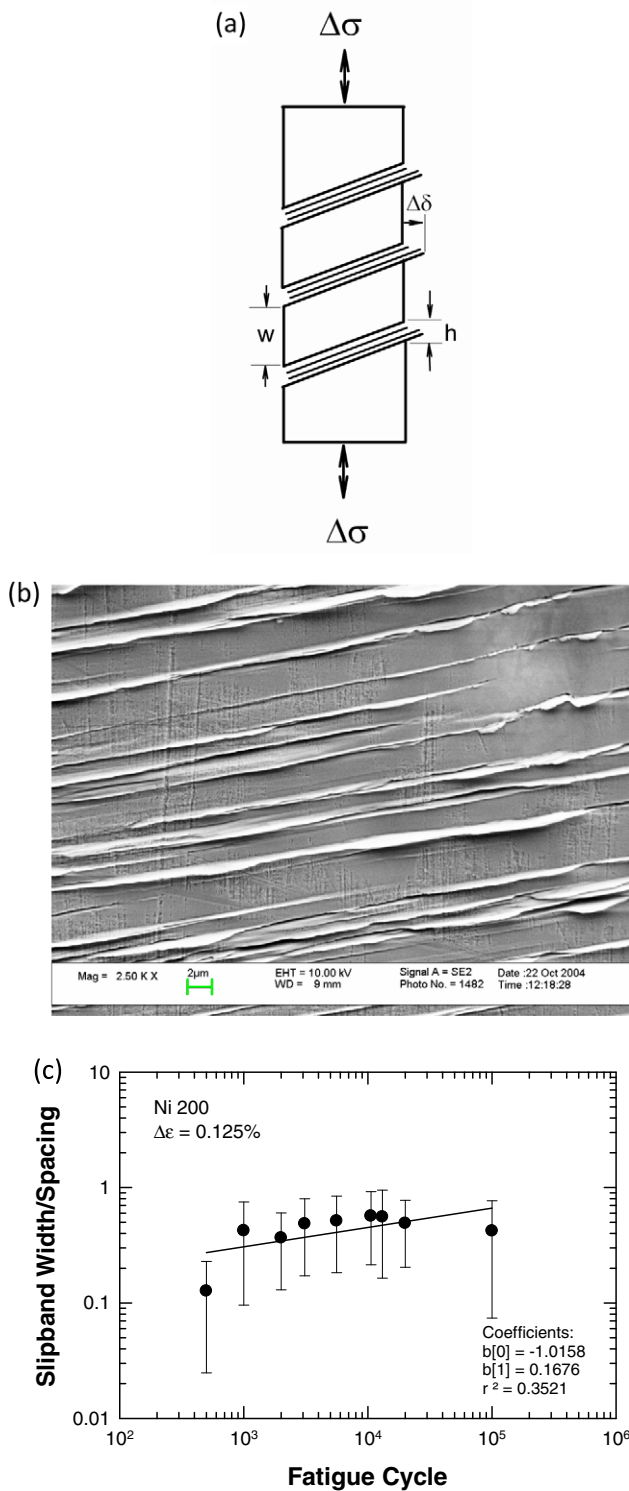
Fig. 2. Evolution of slipband width and spacing of Ni200 during low-cycle fatigue: (a) schematics of slipband width and spacing in an individual grain, (b) SEM micrograph showing PSB in a surface grain in Ni200, and (c) ratio of slipband-width-to-spacing as a function of fatigue cycles for Ni200 tested at $\Delta\varepsilon = 0.125\%$. From Chan et al. [29].

tios were made on grains that were located near the fracture surfaces for strain amplitudes at ±0.125%, ±0.25%, ±0.5%, and ±0.75% in order to investigate the common characteristics of these parameters, if any, near the onset of fatigue fracture. Fig. 3a presents a slipband crack in Ni200 tested at a strain amplitude of ±0.25%. Fig. 3b shows a comparison of the slipband width and spacing at
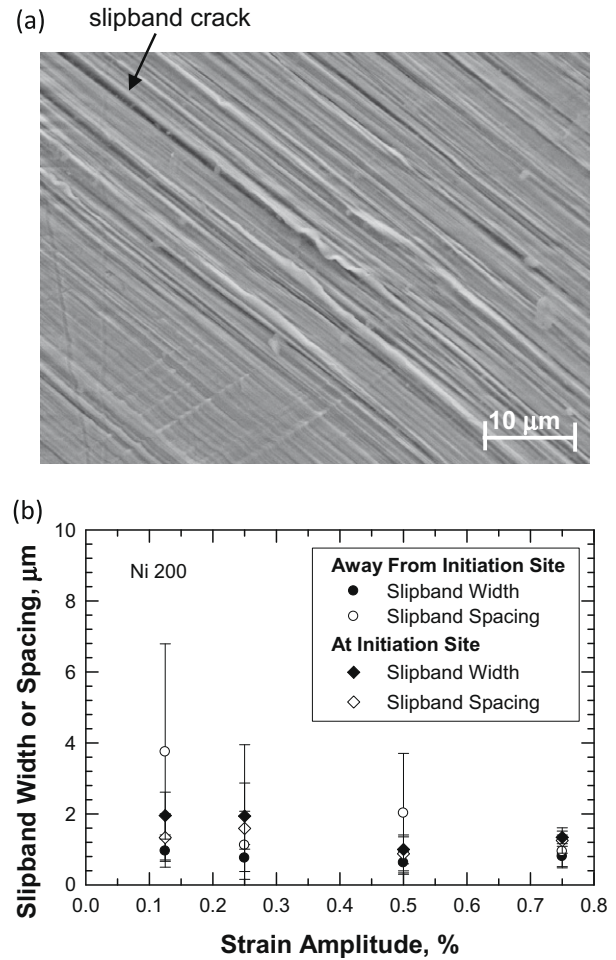
Fig. 3. Crack initiation mechanisms in Ni200: (a) slipband crack and (b) slipband width and spacing at crack initiation near the onset of fatigue fracture. From Chan et al. [29].

various strain amplitudes. The results indicated that in all four cases, the slipband width was on the order of 1 μm and appeared to be relatively insensitive to the strain amplitude. In contrast, the slipband spacing decreased as more slipbands were activated when the strain amplitude increased. At higher strain amplitudes (e.g., ±0.75%), the slipband width and spacing were almost identical, leading to a slipband-width-to-spacing ratio of unity.

A cycle-dependent h/w ratio that manifests a critical value at fracture has important significance in fatigue crack initiation. The significance can be illustrated by recognizing that the accumulation of the shear plastic strain range, $\Delta\gamma_{ps}$, within a slipband is given by $\Delta\gamma_{ps}N$. Assuming that fatigue crack initiation occurs when the accumulated shear plastic strain range value reaches a critical value leads one to [29]

$$\Delta\gamma_{ps}N = C_1 \tag{1}$$

where C_1 is a constant. The macroscopic plastic shear strain range, $\Delta\gamma_p$, of the test specimen is given by

$$\Delta\gamma_p = V_s\Delta\gamma_{ps} = \left(\frac{h}{w}\right)\Delta\gamma_{ps} \tag{2}$$

where V_s is the volume fraction of slipbands within the grains in the test specimen. The plastic strain range, $\Delta\varepsilon_p$, can be related to the plastic shear strain through the Taylor factor, M, leading to

$$\frac{\Delta\varepsilon_p}{M}\left(\frac{w}{h}\right)N = C_1 \tag{3}$$

The correlation results in Fig. 2c suggest that the slipband-width-to-spacing ratio h/w may be related to fatigue cycles according to a power-law given by

$$\frac{h}{w} = C_2 N^{\beta} \tag{4}$$

which, after combined with Eq. (3), leads to the Coffin–Manson equation [30,31] for low-cycle fatigue

$$\Delta \varepsilon_p N_f^{\alpha} = C \tag{5}$$

where $\alpha (=1 - \beta)$ is the fatigue life exponent; $C = MC_1C_2$ is the fatigue life coefficient; N_f is the cycle crack initiation or fracture. The value of the α exponent, which ranges from 0.5 to 1 for most metals, is known to depend on the stacking fault energy [27]. The relation suggests that the value of the fatigue life exponent in the Coffin–Manson equation [30,31] may have its origin in the evolution of the slipband morphology in general and the h/w ratio in particular. This finding is consistent with the experimental observation that the fatigue life exponent varies with the stacking fault energy [27].

2.2. Microstructure-based stress–life relations

Fatigue cracks initiated by the intrusion–extrusion mechanism from persistent slipbands form on the active slip plane that lies at an angle (e.g., 45°) to the stress axis. Most of the slipband cracks have been found to occur in surface grains that are optimally oriented for slip and exhibit a Schmid factor of about 0.5 in Ni-based alloys [9] and in steels [26]. Crack initiation is a complex process that can lead to a crack that is extremely small (≈ 1 μm or less) or one that appears to "pop in" (initiates and rapidly grows) at up to 100 μm long. Planar slip materials are known to concentrate slip and form persistent slipbands that eventually become cracks. Coarse-grained materials are more prone to slipband cracks than fine-grained materials. A number of mechanistic models have been proposed to describe the initiation of fatigue cracks at slipbands or extrusions.

The crack initiation model of Tanaka and Mura [32–34] was based on a dislocation dipole mechanism operating in a surface grain. During fatigue loading, irreversible slip occurs on parallel slip planes in a favorably oriented surface grain, producing dislocation dipoles at the ends of a double pile-up whose coalescence ultimately leads to crack nucleation. Tanaka and Mura's model [32–34] was extended by Chan [35] to explicitly incorporate the microstructural unit length, crack size, as well as other pertinent material parameters in the response equation by considering the energetics of the fatigue crack initiation process. Specifically, the length of the incipient crack was obtained by equating the elastic strain energy released by dislocation coalescence and crack opening to the fracture energy, consisting of elastic and plastic components, required to form the crack surfaces. For fully reverse loading, the stress–fatigue life relation due to Tanaka and Mura can be expressed as [32,36]

$$(\Delta \sigma_R - 2Mk) N_f^{\alpha} = \zeta \tag{6}$$

leading to

$$\sigma_R = \frac{\zeta}{2} N_f^{-\alpha} + Mk \tag{7}$$

where M is the Taylor factor, k is the critical resolved shear stress of the active slip system, N_f is the fatigue life, ζ is the fatigue life coefficient, and α is the fatigue life exponent. The fatigue life coefficient, ζ, for crack initiation at a dislocation pile-up in a grain is given by [36]

$$\zeta = \left[\frac{8M^2 \mu^2}{\lambda \pi (1 - \nu)} \right]^{1/2} \left(\frac{h}{d} \right) \left(\frac{c}{d} \right)^{1/2} \tag{8}$$

where μ is the shear modulus, h is the slipband width, d is grain size, and c is the dislocation pile-up length or the crack size since a dislocation pile-up can be viewed as a shear crack.

In a recent study, the dependence of fatigue life on mean stress, σ_m, was theoretically investigated [36] by considering crack initiation by a dislocation pile-up along a planar slipband in a grain subjected to a cyclic shear stress range $\Delta \tau$, as shown in Fig. 4a. In addition, the mean stress, σ_m, is applied normal to the slipband, as depicted in the stress–strain response shown in Fig. 4b. Since σ_m is normal to the slipband, it has no effect on the slip behavior but is expected to influence the crack initiation process and the subsequent crack growth behavior. The theoretical result indicated that for fatigue under a mean stress, a linear dependence of stress amplitude (σ_a) and mean stress (σ_m) exist at a constant fatigue life as given by [36]

$$\sigma_a = \sigma_R \left[1 - \frac{\sigma_m}{\sigma_{UTS}} \right] \tag{9}$$

where σ_{UTS} is the ultimate tensile strength. Substituting Eq. (7) into Eq. (9) leads one to [36]

$$\sigma_a = \left[\frac{\zeta}{2} N_f^{-\alpha} + Mk \right] \left[1 - \frac{\sigma_m}{\sigma_{UTS}} \right] \tag{10}$$

which is often referred to as the modified Goodman relation [37]. According to Sendeckyj [38], the linear relation between σ_a and σ_m was incorrectly attributed to Goodman [37], as Fidler [39] was the first to report a linear relation between σ_a and σ_m and Haigh [40] was the first to use the straight line representation of constant
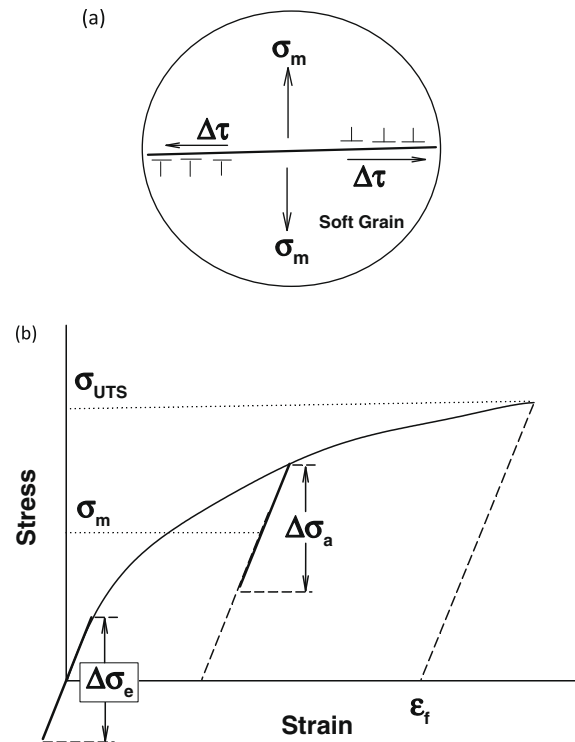

Fig. 4. Schematics of crack initiation under fatigue at a mean stress: (a) schematic shows a dislocation pile-up in a soft grain (primary α) subjected to a shear stress range, $\Delta \tau$, and a mean stress, σ_m, acting normal to the slip plane and (b) a schematic stress–strain curve showing cyclic loading with a stress range, $\Delta \sigma_a$, at a mean stress, σ_m, and the fatigue limit, $\Delta \sigma_e$, for fully reversed loading at zero mean stress ($\sigma_m = 0$). From Chan and Lee [46].

fatigue life data. This linear mean stress dependence shown in Eq. (10) remains valid regardless of the values of the microstructural parameters such as ζ, M, α, and k since these parameters are independent of the mean stress for a specified N_f value [36].

2.3. Effects of microstructure-induced plastic constraint on Goodman diagram

In multiphase alloys, substantial elastic–plastic interactions can occur among constituent grains in the microstructure during cyclic loading due to differences in the critical resolved shear stresses, grain size, and crystallographic orientation of individual phases or constituent components [36]. One particular example is the duplex microstructure in $\alpha + \beta$ Ti alloys, including Ti–6Al–4V, Ti–6Al–2Sn–4Zr–2Mo, and Ti–6Al–6V–2Sn [41–44]. The duplex microstructure is usually obtained by annealing the material in the $\alpha + \beta$ phase field to produce primary α grains. Subsequent cooling at a sufficiently high rate leads to the formation of α lamellae within the remaining β grains to form lamellar or Widmanstatten $\alpha + \beta$ colonies [43,44]. Fig. 5 shows a typical duplex microstructure of Ti–6Al–4V [45]. Since the primary α grains are generally softer than the $\alpha + \beta$ colonies, the duplex microstructure is thus comprised of a two-microconstituent microstructure of soft and hard grains.

Recently, Chan and Lee [46] analyzed the effects of the deformation behaviors of individual phases in Ti-alloys with a duplex microstructure containing a mixture of primary α grains and lamellar $\alpha + \beta$ colonies by applying the finite-element-method (FEM) to the relevant microstructure, of which some of the details are shown in Fig. 6a. The softer primary α grains and the harder lamellar $\alpha + \beta$ colonies were treated as distinct microstructural units with different constitutive properties. The FEM results indicated that the softer (primary α) phase, which reached yielding first, tended to concentrate both the plastic strain and the hydrostatic stress, whose magnitudes depend on the volume fraction of the primary α grains and the load levels. The concentration of hydrostatic stresses in the primary α phase in the duplex microstructure is presented in Fig. 6b.

The hydrostatic stress, σ_m^α, in the primary α phase of a microstructure containing primary α and lamellar $\alpha + \beta$ colonies is comprised of two components: one originated from σ_m due to the external stress state and another induced by the microstructural constraint imposed on the softer primary α phase by the harder lamellar $\alpha + \beta$ colonies. Thus,

$$\sigma_m^\alpha = \sigma_m + \sigma_{mc} \tag{11}$$
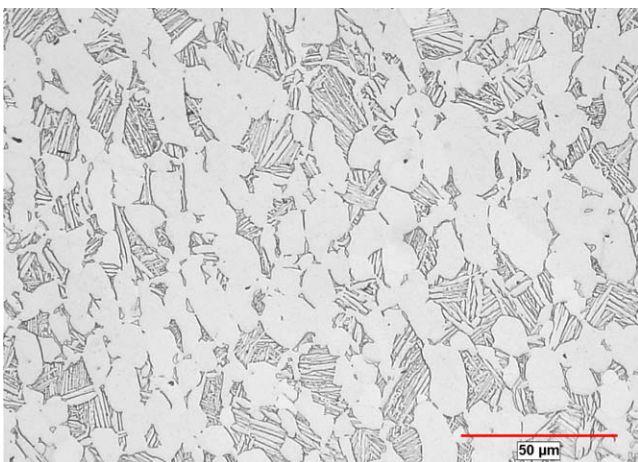

Fig. 5. Duplex microstructure of Ti–6Al–4V with 60% primary α grains (light phase) and 40% of $\alpha + \beta$ Widmanstatten colonies. From Chan and Enright [45].
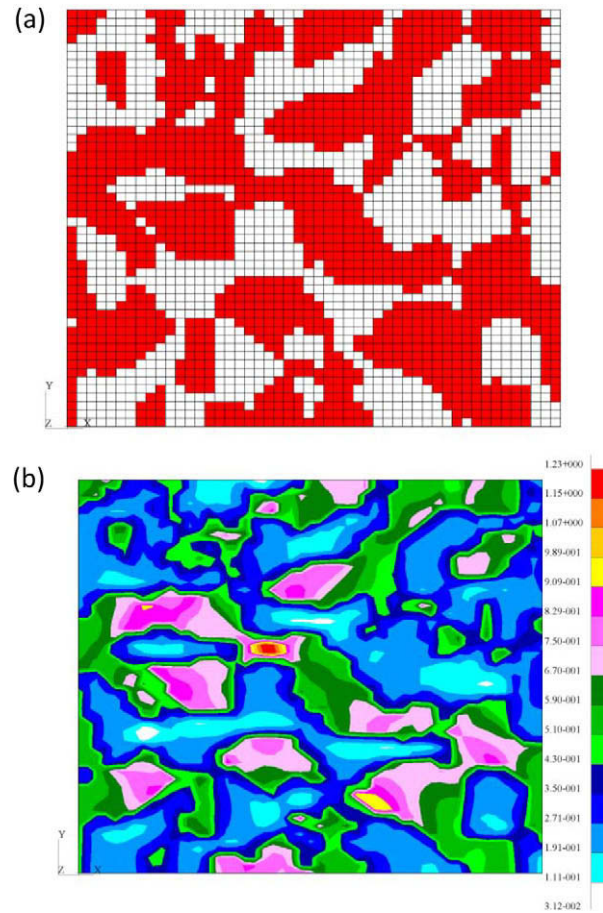

Fig. 6. (a) FE mesh of soft primary α grains (dark) and hard (light) Widmanstatten $\alpha + \beta$ colonies in a duplex microstructure and (b) normalized hydrostatic stress for $V_\alpha = 0.56$ and under plane strain condition at an average stress of 528 MPa. The hydrostatic stress is normalized with respect to the yield stress of individual phases. From Chan and Lee [46].

where σ_{mc} is the mean stress induced in the softer grains. Eq. (10) can be combined with Eq. (11) to give [46]

$$\sigma_a = \left[\frac{\zeta}{2}N_f^{-\alpha} + Mk\right]\left[1 - \frac{\sigma_m}{\sigma_{UTS}} - \frac{\sigma_{mc}}{\sigma_{UTS}}\right] \tag{12}$$

which indicates that bilinear mean stress dependences occur in the presence of microstructure-induced plastic constraint, σ_{mc}. The higher plastic strain and hydrostatic stress renders the softer phase more prone to crack nucleation by high-cycle fatigue than the harder phase. FEM analysis of the duplex microstructure of primary α grains with $\alpha + \beta$ Widmanstatten colonies (lamellar colonies) suggested that the microstructurally-induced hydrostatic stress is given by [46]

$$\sigma_{mc} = qV_\alpha^2(1 - V_\alpha)\sigma_m \tag{13}$$

where V_α is the volume fraction of primary α grains and q is a constant representing the plastic interaction between the primary α grains and lamellar $\alpha + \beta$ colonies. Substituting Eq. (13) into Eq. (12) leads one to [46]

$$\sigma_a = \left[\frac{\zeta}{2}N_f^{-\alpha} + Mk\right]\left[1 - \frac{\sigma_m}{\sigma_{UTS}}\left[1 + qV_\alpha^2(1 - V_\alpha)\right]\right] \tag{14}$$

which indicates that the linear dependence between stress amplitude and mean stress of the modified Goodman relation, Eq. (10), is altered by the presence of microstructurally-induced constraint in the softer primary α grains. In particular, the microstructure-in-

duced hydrostatic stress reduces the mean stress required to cause ultimate fracture in the primary α phase and leads to bilinear relations between σ_a and σ_m, as shown in Fig. 7. At low mean stresses, the linear relation exhibits a steeper slope and describes the dependence of σ_a on mean stress for the primary α phase. At higher mean stresses, the primary α grains are cracked and the second linear relation, which describes the σ_a and σ_m relation of the lamellar $\alpha + \beta$ colonies, is given by [46]

$$\sigma_a = (1 - V_\alpha)\sigma_e^L \left[1 - \frac{\sigma_m}{\sigma_{UTS}} \right] \tag{15}$$

where σ_e^L is the fatigue limit of the lamellar $\alpha + \beta$ colonies for fully reverse loading. According to Eqs. (14) and (15), the plastic interactions between the primary α grains and the lamellar $\alpha + \beta$ colonies lead to different hydrostatic stresses in individual microstructural units which are then manifested as different mean stress dependence of the fatigue limits.

It is well-documented that Ti-alloys exhibit two different mean stress dependences which vary with microstructure [41,42,47–51]. A linear dependence between σ_a and σ_m has been observed in α-Ti [47,48], β-Ti [47,48], and fully lamellar $\alpha + \beta$ Ti alloys [47,48,50,51]. In contrast, near-α and $\alpha + \beta$ Ti alloys with a duplex microstructure consisting of primary α grains and lamellar $\alpha + \beta$ colonies manifest an anomalous mean stress sensitivity and deviations of σ_a below the Goodman line (negative deviations) [47,48,50,51]. For example, experimental data of Ti–6Al–4V [50,51], shown in Fig. 8, show a linear relation between σ_a and σ_m for the lamellar $\alpha + \beta$ microstructure. For duplex microstructures with primary α grains and lamellar $\alpha + \beta$ colonies, non-linear σ_a and σ_m relations with negative deviations ($\sigma_a <$ Goodman line at a given σ_m) from the Goodman line are observed. For Ti–6Al–4V alloy with a duplex microstructure, the reduction of σ_a due to the constraint effect is a non-linear function of the volume fraction of the primary α grains in the microstructure [45].

2.4. Microstructural influence on S–N_f curve

Fatigue crack initiation life depends on a number of microstructural parameters in a complicated manner. According to Eqs. (10) and (12), fatigue crack initiation is favored in grains with a low value of the Taylor factor. The lowest value of Taylor factor is 2 and it corresponds to a Schmid factor of 0.5. Several studies have shown that slipband crack initiation in coarse-grained Ni-based alloys
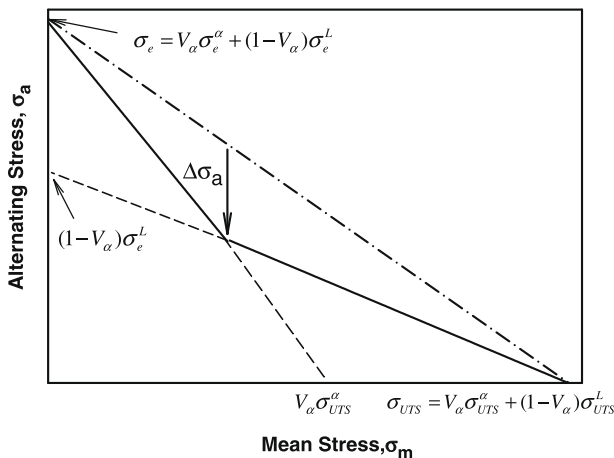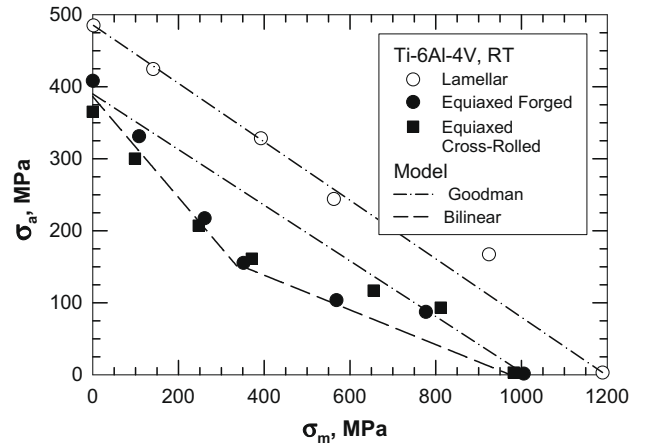
Fig. 8. A comparison of plots of stress amplitude, σ_a, versus mean stress, σ_m or Ti–6Al–4V with a fully lamellar $\alpha + \beta$ microstructure (open circles) or a duplex microstructure with 85 vol.% primary α gains and 15% lamellar $\alpha + \beta$ colonies (filled circles and squares). Figure is from Chan [36] and experimental data are from Ivanova et al. [50].

predominantly occurred in surface grains that were optimally oriented for slip and exhibited a high Schmid factor close to 0.5 [9]. On the other hand, crack initiation in surface grains with a lower Schmid factor was also observed [9], indicating the crystallographic orientation was not the only microstructural parameter affecting the crack initiation process.

The important role of grain size in fatigue crack initiation is well established and can be predicted on the basis of Eqs. (10) and (12). In general, fatigue crack initiation is favored in coarse-grained material compared to fine-grained materials, assuming everything else is equal. It is also well-documented that crack initiation life increases and crack propagation life decreases with decreasing grain size for microcrystalline materials. These general trends are also applicable in nanocrystalline Ni with a 30 nm grain size and in ultrafine-grained Ni (100 nm to 1 μm grain size) [52,53]. Hanlon et al. [52,53] showed that grain refinement resulted in improvements in the S–N_f response and increases in the fatigue limit, but reduction in the FCG resistance due to higher fatigue crack growth rates and decreases in the FCG threshold. A recent study [54] indicated in Ti-6246 with a duplex microstructure, fatigue crack initiation occurred in primary α grains in which grain sizes were larger than average grain size and tilted toward the largest grain size tail of the grain size population, even though the largest grain may not always initiate a fatigue crack. The finding appears to reinforce the notion that more than one microstructural parameter influences the crack initiation process.

Texture may enhance fatigue crack initiation if groups of grains are oriented for easy slip within the applied stress field. In some alloys, the apparent grain size may not be an accurate view of the effective "grain size" characterizing the slip distance. An example of this phenomenon is a ferritic–pearlitic steel, where the underlying alpha grain has only one crystallographic orientation [55], or a grain existing in the gamma phase before a martensitic transformation, which is larger than any dimension in the transformed structure. Besides steels, textural influences also exist in many Ti-alloys [54,56]. For example, prior β grains in $\alpha + \beta$ Ti alloys transform to groups of similarly oriented $\alpha + \beta$ lamellar colonies that exhibit similar slip behavior and easy slip transmission across colony boundaries. Therefore, the effective slip distance of the similarly oriented $\alpha + \beta$ lamellar colonies is the size of the prior β grains and not the smaller lamellar colony size [54,56]. A group of similarly oriented grains that exhibit cooperative slip behavior over a distance larger than the characteristic distance of individual grains

Fig. 7. Schematic illustrating the reduction of the alternating stress, σ_a, by microstructure-induced hydrostatic stress that leads to bilinear HCF failure curves for the softer primary α grains and the harder lamellar $\alpha + \beta$ colonies in Ti–6Al–4V with a duplex microstructure. From Chan and Lee [46].
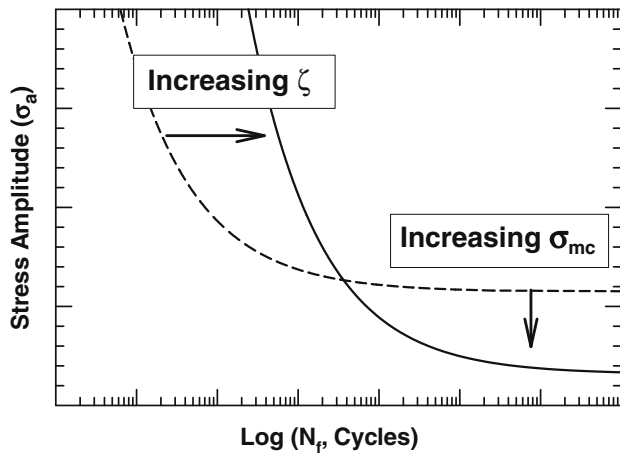
Fig. 9. Competing effects of increasing the ζ value and microstructure-induced plastic constraint, σ_{mc}, accompanied with the transition from surface-grain crack initiation to interior-grain crack initiation. From Chan [36].

is often referred to a supergrain [1,57], whose larger slip distance often leads to easy crack initiation and results in lower fatigue life.

In the absence of defects, fatigue crack initiation tends to occur at surface grains which are optimally oriented for slip by virtue of a low Taylor factor of $M = 2$. In the interior grains, the Taylor factor is generally higher because of the activation of multiple slip systems,
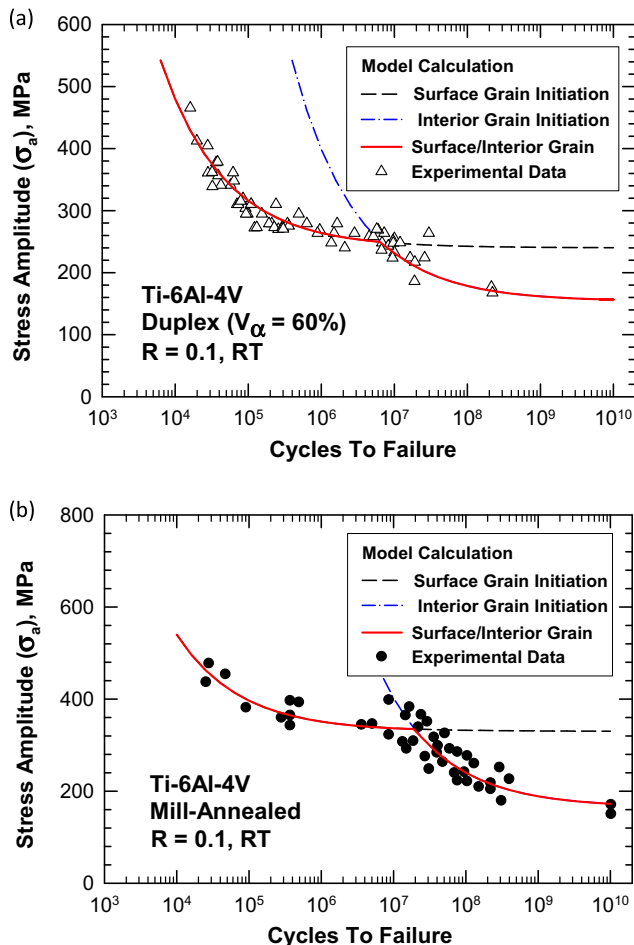

Fig. 10. Comparisons of calculated and measured σ_a–N_f curves with double fatigue limits for Ti–6Al–4V: (a) duplex microstructure and (b) mill-annealed microstructure. From Chan [36]. Experimental data of the duplex material are from [58–60] and those of the mill-annealed material are from [49].

some of which may not be oriented for optimal slip. The increase of the Taylor factor (M) has the effect of shifting the fatigue life to higher stress amplitude and longer life. The increase in slip uniformity causes an increase in the ζ value via Eq. (10) and a shift of the σ_a–N_f curve to longer fatigue lives via Eq. (12), as shown in Fig. 9 [36]. In the case of a duplex microstructure, the softer phase in the interiors is also subjected to a microstructure-induced constraint stress that reduces the σ_a at a given mean stress and leads to bilinear σ_a–σ_m relations. In contrast, the reduction of σ_a by σ_{mc} results in a lower fatigue limit in a plot of σ_a–N_f curve, as illustrated in Fig. 9. Thus, the transition of fatigue crack initiation from surface grains to interior grains can drastically alter the mean stress dependence and leads to the mean stress anomaly [41,42], and an over-prediction of HCF fatigue strength if linear mean stress dependence is tacitly assumed. Since the M and σ_{mc} terms in Eq. (12) produce opposite effects, a range of fatigue life behavior and a high degree of variability can be expected, including multiple apparent fatigue limits, which are depicted in Fig. 9. The σ_{mc} term is expected to dominate when the volume fraction of primary α phase in the duplex microstructure is substantial. e.g., $V_\alpha = 60$–80% in Ti–6Al–4V [45].

Double fatigue limits have been observed in Ti–6Al–4V with the duplex microstructure [38,58–60] and the mill-annealed microstructure [61]. The S–N_f curves of these two alloys resemble that shown in Fig. 1a. Applications of Eq. (12) to the fatigue data of these two microstructures are presented in Fig. 10a and b, respectively. The double fatigue limits (one apparent and one true) were accompanied by a change of fatigue mechanism from surface-grain initiation to interior-grain initiation [48,61]. According to Eq. (12), the double fatigue limits are caused by two competing effects: (1) an increase in the ζ value due to higher M and slip morphology in the interior grains, and (2) a higher microstructure-induced plastic constraint, σ_{mc}, in the interior grains. The concentration of hydrostatic stresses and plastic strains in soft grains, which accompany a high σ_{mc}, leads to both bilinear mean stress dependences in a σ_a–σ_m plot and double fatigue limits in a σ_a–N_f curve.

2.5. Microstructural influence on Kitagawa diagram

Kitagawa diagram is a double logarithmic plot of stress range versus crack length that depicts the limiting stress against crack initiation and the growth of a large-crack [62]. Such a plot is usually constructed by plotting the fatigue limit, usually taken at a fatigue life of 10^7 cycles, as a horizontal line from an arbitrarily small initial crack length (e.g., 1 μm) up to the small-crack limit, a_0. This horizontal line represents the limiting stress below which fatigue crack initiation does not occur. The large-crack growth boundary is a slanted line with a slope of $-1/2$ that intersects the endurance limit line at a_0. A fatigue crack with a length greater than the slant boundary has a ΔK larger than the large-crack threshold and can grow to failure.

The occurrence of crack initiation at stress ranges below the conventional HCF fatigue limit requires the addition of a horizontal boundary in the Kitagawa diagram to represent the endurance limit at UHCF. In addition, the growth of small cracks below the large-crack threshold requires the addition of a slant boundary to represent the intrinsic FCG threshold for the softer grain. These changes of the Kitagawa diagram are depicted in Fig. 11 [36]. The addition of these two boundaries creates a regime where microcracks are initiated and arrested. Once initiated, the fatigue cracks can remain dormant without subsequent growth when the crack lengths are small and the stress intensity factors are below the intrinsic FCG threshold. The non-propagation region, which is shown as Region NP in the Kitagawa diagram [62] in Fig. 11, accumulates fatigue damage by nucleating more fatigue cracks that coalesce with existing cracks until the crack length is sufficiently long that the intrin-
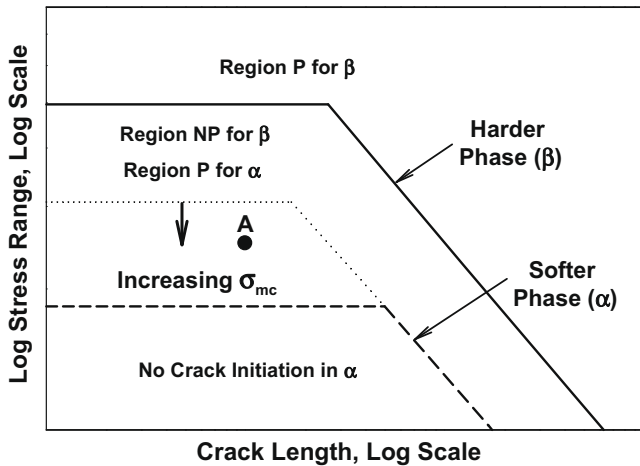
Fig. 11. A schematic Kitagawa diagram illustrates the lowering of the fatigue (endurance) limit of the softer (primary α) phase due to microstructure-induced plastic constraint, σ_{mc}, in a two-phase microstructure. A stress range at Point A becomes susceptible to crack initiation in primary α after the fatigue limit is lowered. At stresses within the dotted lines, fatigue damage in the soft phase (α) proceeds by crack initiation and coalescence until the crack length exceeds the growth threshold boundary indicated by the slanted dotted line. From Chan [36].

sic threshold is exceeded [56,63]. Then the small cracks can potentially propagate to become large-cracks and the critical length for fracture to occur. The region where fatigue cracks can propagate to failure is indicated as Region P in Fig. 11. For stress ranges below the UHCF endurance limit, crack initiation does not occur unless assisted by the stress concentration factor of a defect in the microstructure. This process of fatigue crack initiation and coalescence

to form a microcrack in a supergrain, which is illustrated schematically in Fig. 12, has been observed in several $\alpha + \beta$ Ti alloys with a duplex microstructure.

The plastic interaction stresses associated with soft primary α grains and hard Widmanstatten colonies in $\alpha + \beta$ Ti alloys are tensile and compressive, respectively [46]. At a scale that encompasses both soft and hard grains, the interaction stresses may cancel each other such that their respective effects on fatigue life can be nullified. These interaction stresses can also cancel out at length scales larger that the sum of the dimensions of these microstructural features. On this basis, it can be expected that the interaction stresses affect fatigue crack initiation and the growth of small cracks which small plastic zone size interrogates a length scale on the order of one grain-size or less. As the crack length increases, the plastic zone interrogates a larger number of grains, and the probability that the compressive and tensile interaction stresses cancel each other increases. The consequence is that the effects of microstructure-induced constraint stresses are likely to be lessened as the crack length increases and the plastic zone engulfs a sufficient number of grains to behave more like a continuum. Thus, the interaction stresses are expected to predominantly affect the fatigue life in the high-cycle fatigue and ultra high-cycle fatigue regimes where crack initiation and early growth of small cracks dominates and could have lesser effects in the LCF region where continuum crack growth dominates.

2.6. Slip-induced grain boundary initiation

Besides intrusions and extrusions, fatigue crack initiation can occur at grain boundaries and twin boundaries as the result of slip impingement [4–6]. In the absence of grain boundary segregation
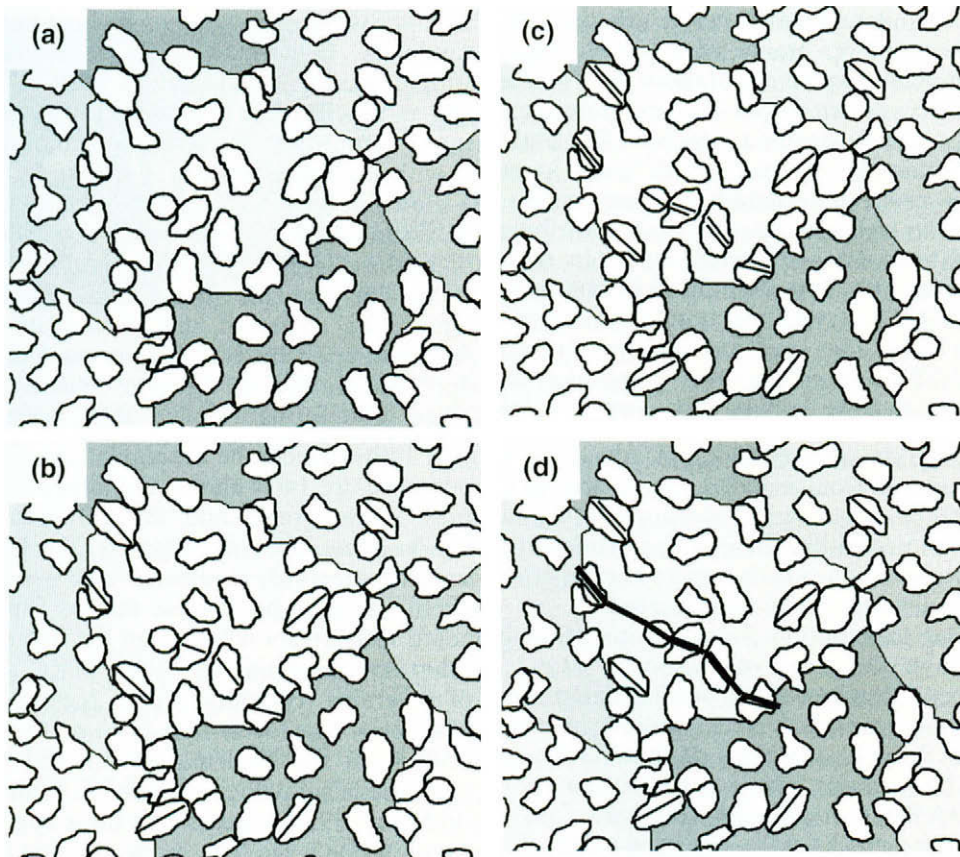
Fig. 12. A schematic depiction of the crack initiation and coalescence process in primary α grains to form a microcrack in a prior β grain that acts like a supergrain in an $\alpha + \beta$ Ti alloy with a duplex microstructure: (a) primary α grains in a prior β grain, (b) slip in primary α grains, (c) slipband cracks in primary α grains, and (d) linking of slipband cracks to form a microcrack across the prior β grain. From Szczepanski et al. [54].

and environment effects, fatigue cracks can initiate at high-angle grain boundaries that lie close to normal to the tensile stress and at grain boundaries that exhibit large misorientation angles or are impinged by localized slipbands [57]. In particular, fatigue cracks are initiated when slip causes steps along grain boundaries. In general, fatigue cracks initiate at grain or twin boundaries where impinging slip causes plastic incompatibility and stress concentration. Furthermore, grain boundary initiation is more prevalent at high strains than at low strains [29].

The tendency of grain boundary cracking relative to slipband crack was reported for Ni200 at several strain amplitudes [29]. Fatigue crack initiation at low strain amplitudes (±0.125% and ±0.25%) occurred by decohesion along slipbands, as illustrated in Fig. 13a. At a strain amplitude of ±0.5%, fatigue cracks initiated

from either slipbands or at grain boundaries. At ±0.75% amplitude, fatigue cracks initiated mostly from grain boundaries as shown in Fig. 13b, although slipband cracks were observed occasionally. A significant observation of the results shown in Fig. 13a and b is that most of the slipband cracks lie within individual grains and often stop at grain boundaries. In contrast, most of the grain-boundary cracks extend to occupy several grain-boundary facets, rather than confining to a single grain boundary. Fig. 13c shows that the percentage of fatigue cracks formed along slipbands decreases with increasing strain amplitudes. At ±0.125% strain amplitude, about 90% of the fatigue cracks were slipband cracks. The percentage decreased to 13% at a strain amplitude of ±0.75%. The corresponding values of slipband width and spacing for fatigue crack initiation at various strain amplitudes are shown in Fig. 3b, which shows that the slipband-width-to-spacing approaches unity when fatigue crack initiation occurred regardless of the crack type.

Studies on Waspaloy [57,64] revealed that fatigue crack initiation occurred at both slipbands and grain boundaries under cyclic loading at a maximum stress corresponding to 85–95% of the yield strength. The crack initiation sites were grains with a size larger

Fig. 13. Crack initiation mechanisms in Ni200: (a) decohesion along slipbands, (b) grain-boundary cracking, and (c) relative percentage of slipband and grain-boundary cracks at various strain amplitudes. From Chan et al. [29].
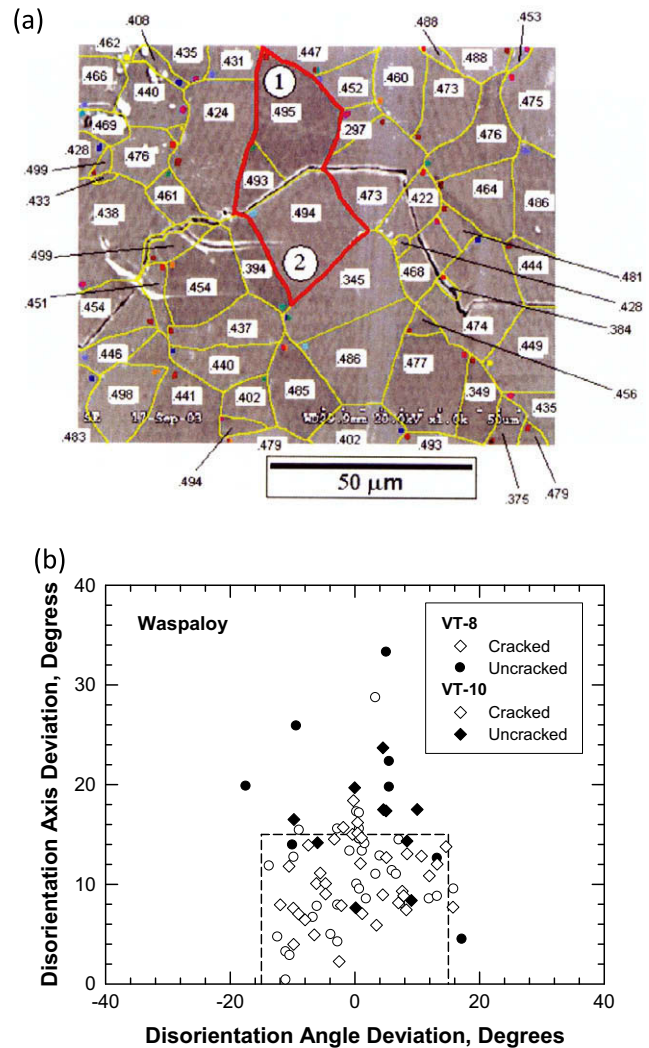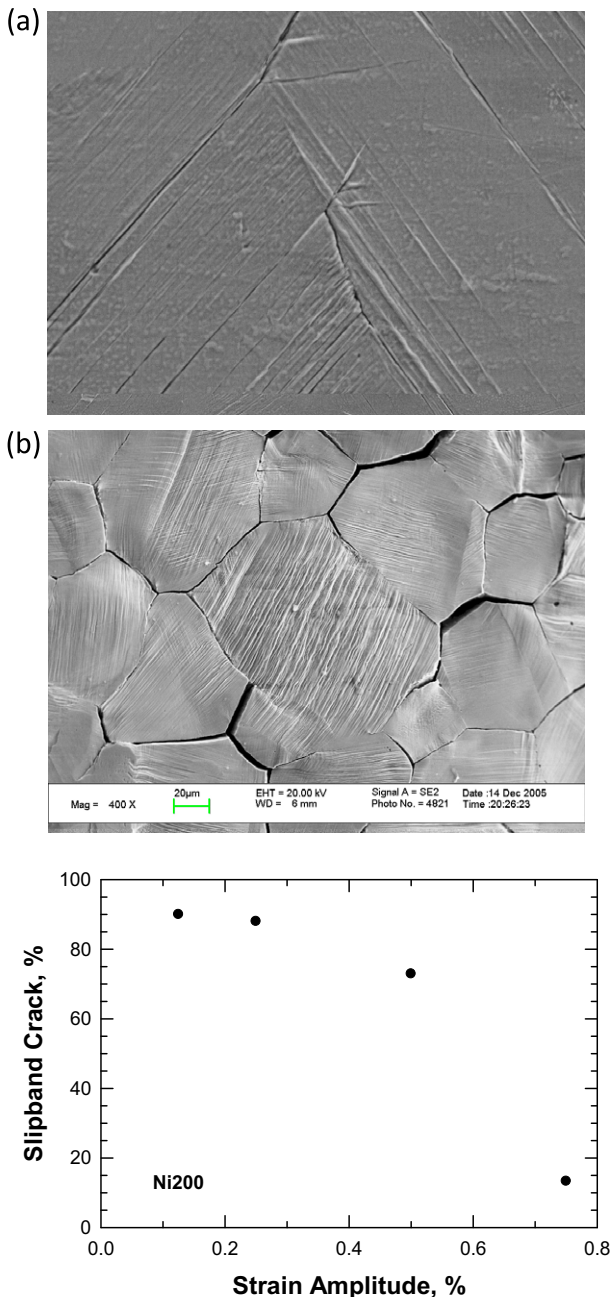

Fig. 14. Crack initiation in grain clusters in Waspaloy: (a) a grain cluster with similar Schmid factor (circled in red) and grain-boundary cracks initiated by LCF [64] and (b) plot of disorientation angles indicating fatigue crack initiation is favored in grain clusters with disorientation angles that are less than 15° [57]. (For interpretation of the references to colour in this figure legend, the reader is referred to the web version of this article.)

than the average grain size, but not necessarily the largest grains. The initiation site was located in a cluster of grains that exhibited similar Schmid factors. The grain clusters, shown in Fig. 14a [64], that initiated fatigue cracks exhibited low-angle boundaries with an angle of misorientation less than 15°, as shown in Fig. 14b [57]. In contrast, clusters with misorientation higher than 15° did not initiate fatigue cracks, Fig. 14c. Furthermore, grain boundaries were more likely to crack when impinged by slipbands at an angle larger than about 72° [57]. These findings suggested that fatigue crack initiation in Waspaloy appeared to occur in a "supergrain", i.e., a cluster of grains with similar crystallographic orientation that enables easy slip transmission across low-angle grain boundaries. Such a grain cluster also acts like a single grain with an effective slip distance that is larger than the average grain size. The implication is that local texture is important for crack initiation and its influence can manifest as a neighborhood effect by adjacent grains. Besides Ni-based alloys, the "supergrain" phenomenon has also been observed in Ti-alloys [54,56], as alluded to earlier in proceeding section.

3. Crack initiation at pores

Fatigue crack initiation at pores is fairly common in cast alloys [65–71] and in powder-metallurgy alloys [12]. In cast Al- and Mg-alloys, the casting pores can be gas pores which are typically round, and shrinkage pores which typically exhibit a more complex geometry, including sharp radii and crack-like features [65–71]. In Al alloys such as A356 and B319, which are used as engine block materials, shrinkage pores are usually located near or at grain boundaries, often accompanied by the presence of oxide films and brittle intermetallic phases [67,71]. Fig. 15a and b shows examples of shrinkage pores in B319 and A356 castings, while Fig. 15c and d depicts fatigue crack initiation at casting pores in these two cast materials [71].

The fatigue life in Al castings is significantly affected by the crack initiation site. In particular, fatigue failure can originate from porosity, oxide films, inclusions, intermetallic phases, Si particles, and slipbands [66,67]. In general, crack initiation at persistent slipbands occurs only at low or essentially zero porosity. Crack initiation at pores generally dominates when the pore size or porosity exceeds a critical level in Al castings. A comparison of the Weibull plots of fatigue life data for Sr-modified A356 Al, shown in Fig. 16 [66], indicates that fatigue failure is controlled mostly by porosity, followed by oxide film, and then persistent slipband. Both the fatigue strength and the fatigue life are reduced with increasing the pore size. Many investigators showed that fatigue life decreases with increasing pore areas and is dominated by fatigue crack growth [69]. For most cases, fatigue cracks initiated from pores located at or near the surfaces [67–69]. Fig. 17a shows the distribution of initiation pore size in E319 Al castings tested at two
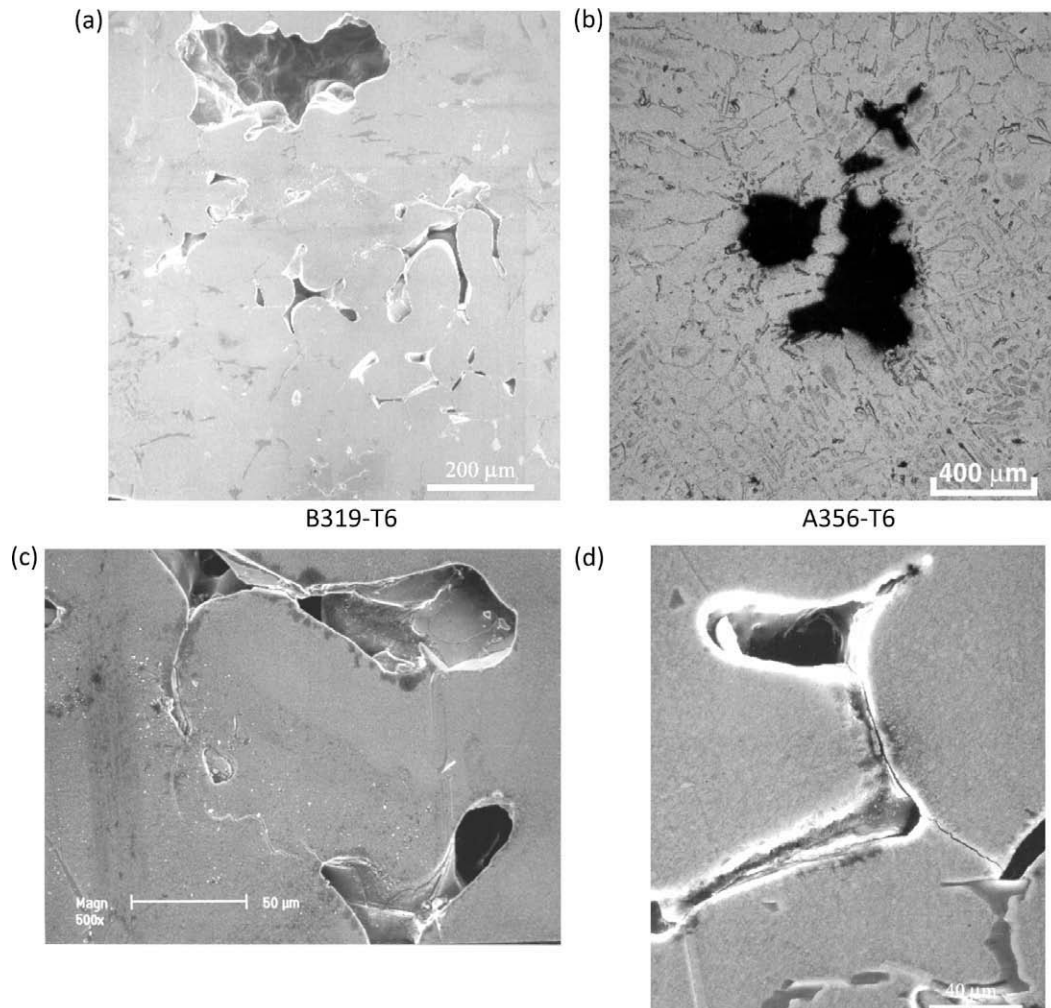
Fig. 15. Pore morphology: (a) large rounded gas pores and shrinkage pores with sharp radius of curvatures in B319–T6 and (b) large rounded gas pores in A356–T6. Fatigue crack nucleation at casting pores and propagation around a dendrite arm in B319–T6: (c) cracks grew around a dendrite arm and (d) fatigue cracks linked casting pores and debonded Si particles by propagating along apparent interdendritic boundaries. The loading axis is horizontal in (c), but is vertical in (d). From Chan et al. [71].
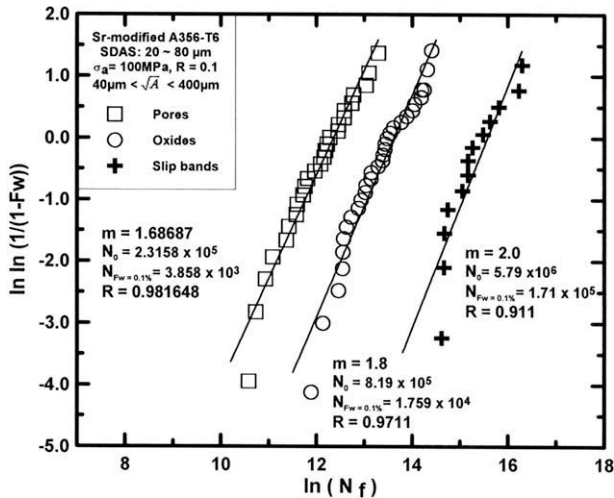
Fig. 16. Weibull plots of fatigue life data of Sr-modified A356 castings exhibiting crack initiation sites at pores, oxides, and slipbands. From Wang et al. [66].

frequencies. The corresponding S–N_f curves are shown in Fig. 17b [69]. Because of the presence of relatively large pores, the fatigue life of E319 Al castings is dominated by crack growth, even in the very high-cycle regime [69].

In gigacycle fatigue, fatigue crack initiation in a cast Al alloy occurs at pores located at or near the surface [68]. The maximum pore size was less than 120 μm and it appeared to exert minimal effects on fatigue life. The fatigue life increases with decreasing stress amplitude without an endurance limit at 1×10^9 cycles. In contrast, fatigue crack initiation in a cast Mg alloy (hot-pressed AZ91) occurs at pores located at or near the surface [68]. Despite the presence of pores, hot-pressed (hp) AZ91 exhibits an endurance limit at 1×10^9 cycles [68]. Fig. 18 compares the S–N_f curves of cast Al and Mg alloys [68]. The difference in fatigue behavior in the various cast alloys appears to be related to the pore size. A number of investigators reported that fatigue life decreases as the size of the crack initiation pores are increased [67]. Below a critical pore size, the fatigue strength of pore-containing castings is similar to those that are isostatically pressed and pore-free. For Sr-modified A356 alloys, the critical pore size is about 25 μm [67].

The influence of pore size, spacing, and clustering on fatigue crack incubation, which includes crack formation and the growth of the small crack within the local strain field of the pore, has been analyzed by Fan et al. [72] using an FEM-based micromechanical approach. Using a cluster of four pores of selected sizes and spacing, Fan et al. [72] computed the local strain amplitudes in the pore-containing specimen subject to various stress amplitude. The local strain amplitudes were used to estimate the cycles to crack incubation using either the Coffin–Manson equation [30,31] or the Fatemi–Socie critical plane criterion [73]. As expected, larger pores concentrate higher plastic strain and lead to a lower fatigue crack incubation life [72]. Similarly, smaller pore spacing allows more pore interaction, leading to higher strain concentration and lower incubation life. There is also a competition between the effects of pore size and spacing size on plastic strain intensification [72]. The plastic strain intensification effect is sensitive to the applied stress level and is more severe at stress amplitudes below macroscopic yielding [72].

Most, if not all, of the fatigue analyses of cast alloys in the literature rely on large-crack fracture mechanics and fatigue crack growth data. In many instances, the pore areas are considered cracked areas and utilized in the estimation of the fatigue life. More often than not, these analyses showed that fatigue crack
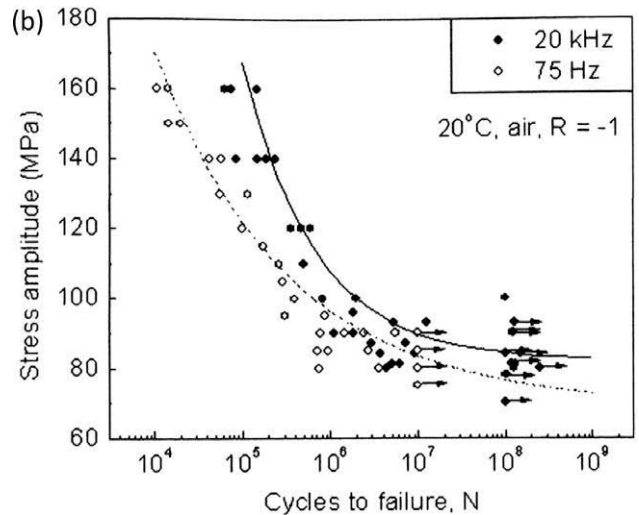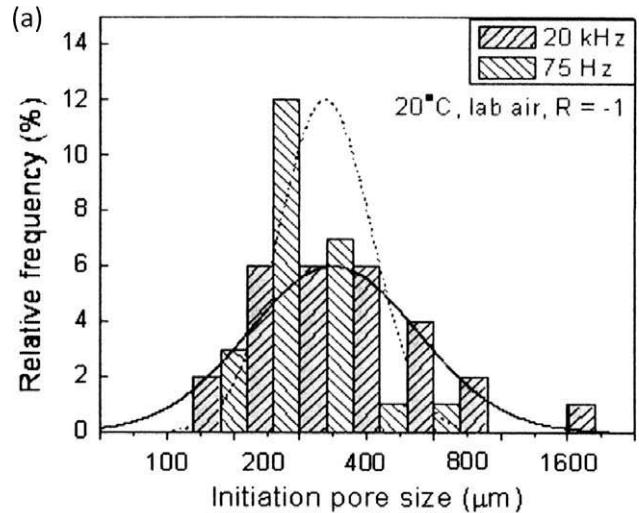
Fig. 17. Initiation pore size distribution and S–N_f curves for E319 Al castings at two test frequencies: (a) pore size distribution and (b) S–N_f curves. Fatigue life is dominated by FCG due to large pore size. From Zhu et al. [69].

Fig. 18. Comparison of S–N_f curves for AlSi7Mg0.3 and Az(1 hp in air at 20 °C. From Mayer et al. [68].

growth dominates the fatigue life of cast alloys with porosity levels exceeding a critical level of pore size or porosity and the fatigue

Fig. 19. Worst-case notch concept showing: (a) limiting threshold stress with increasing notch stress concentration and (b) threshold stress versus crack size and notch severity characterized in terms of notch root radii, $\rho_1 < \rho_2 < \rho_3$, for a constant notch depth. From Hudak et al. [74].

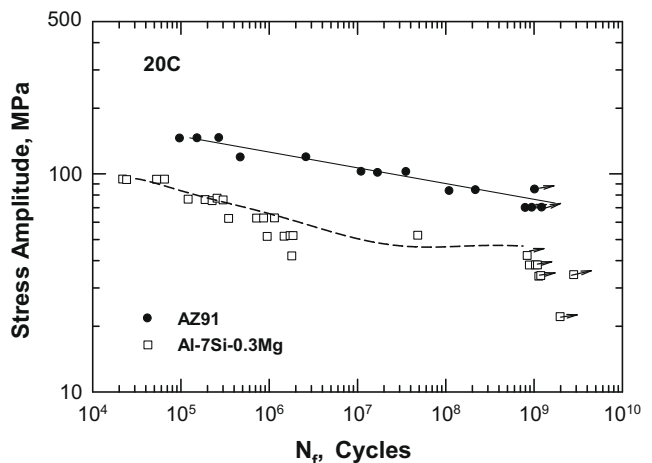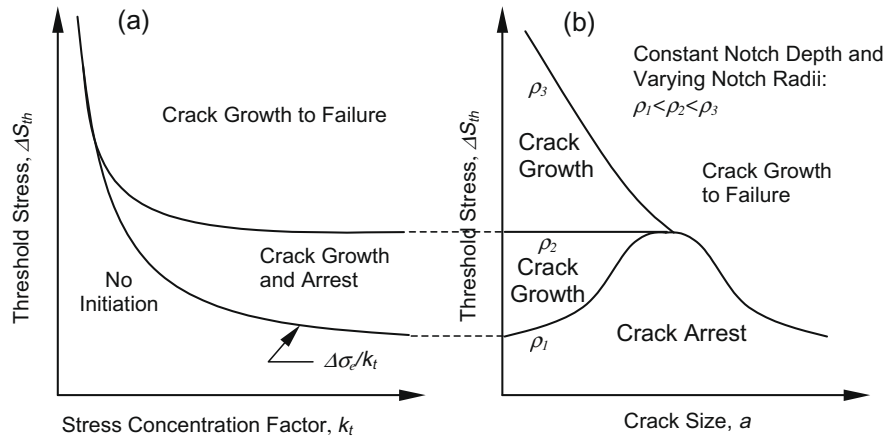strength can generally be predicted on the basis of the large-crack fatigue crack growth threshold. While this approach captures most of the experimental observations on the $S-N_f$ behavior of cast alloys, it fails to address the presence of double or dual fatigue limits and the transition from surface initiation to subsurface initiation in some cast alloys. To account for these two observations, the stress concentration effects by the pores and the corresponding stress gradients must be considered in the fatigue crack growth analysis. One particular analysis that is applicable to treat stress concentration of pores and pore-induced fatigue failure is the worst-cast notch analysis [74], which treats the initiation and growth of a fatigue crack under the influence of the stress field of a notch, by assuming a pore in a cast alloy can be approximated as a micro-notch. The "worst-case notch" concept is illustrated in Fig. 19 [74] where the nominally applied threshold stress for a notched member is shown as a function of both the elastic stress concentration factor k_t and crack size 'a'. As can be seen in Fig. 19a, the threshold stress, computed by dividing the endurance limit ($\Delta\sigma_e$) by k_t, continually decreases with increasing k_t (and notch severity). However, worst-case notch theory predicts a limiting k_t, termed k_w, above which further increases in k_t no longer result in decreases in the threshold stress due to the occurrence of crack arrest and non-propagating cracks. These curves define boundaries separating three distinct regimes where: (1) crack initiation will not occur; (2) crack initiation will occur, followed by crack arrest; and (3) crack initiation followed by crack growth will result in failure of the notched member. These same regimes are shown as a function of crack size in Fig. 19b, for a fixed notch depth and three different notch root radii, ρ_1, ρ_2, ρ_3. As indicated in Fig. 19b, the threshold stress increases as the radius increases and there exists a limiting radius, ρ_w, above which crack arrest cannot occur. In general, the notch severity will be a function of both notch depth, b, and notch root radius, ρ, thus the failure boundaries in Fig. 19b will move with varying notch depth. However, since this dependence can be computed using fracture mechanics, the worst-case notch can always be defined.

In general, the threshold stress is a function of the notch or pore geometry, loading mode, and material variables as follows [74]

$$\Delta S_{th} = \Delta S_{th}(k_t[b, \rho], a, a_0, \lambda) \tag{16}$$

where λ is a parameter which depends on loading mode (e.g., tension versus bending) and a_0 is the small crack parameter suggested by El Haddad et al. [75]. Application of the worst-case notch approach to low-carbon steel is illustrated in Fig. 20, which is based on calculations for the case of an edge notch in a low-carbon steel containing a through-thickness crack ($F = 1.12$) under remote load-
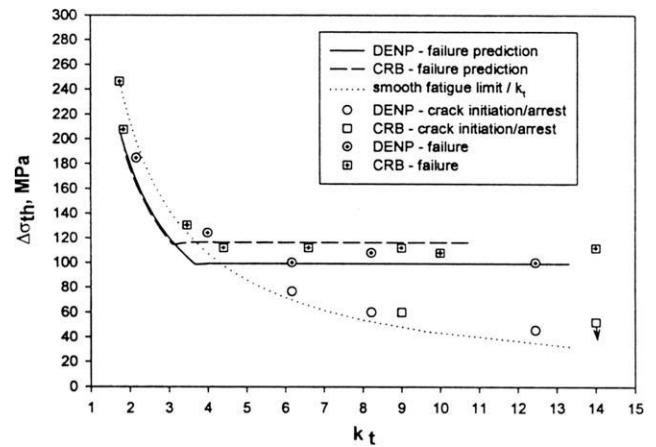
Fig. 20. Comparison of worst-case notch prediction with notched steel HCF data showing the existence of a threshold stress (solid and dashed lines) controlled by FCG and a threshold stress controlled by crack initiation (dotted line). The worst-case threshold stress depends on the notch geometry and the small-crack growth threshold. From Hudak et al. [74].

ing at $R = 0$ [74] using fatigue properties given in [76]. In general, these model calculations suggest the occurrence of three major processes that govern the predicted value of ΔS_{th}. First, when the initiated cracks are vanishingly small, the value of ΔS_{th} is governed by "crack initiation" and can be determined using the classical $S-N_f$ endurance approach. Here ΔS_{th} is simply given by the endurance limit divided by the elastic stress concentration factor, leading to [74]

$$\Delta S_{th} = \frac{\Delta\sigma_e}{k_t} \tag{17}$$

Second, when the initiated cracks are very long, ΔS_{th} is governed by the long-crack threshold, ΔK_{th}, and according to classical fracture mechanics theory is given as [74]

$$\Delta S_{th} = \frac{\Delta K_{th}(R)}{F\sqrt{\pi(b+a)}} \tag{18}$$

Under the above conditions, the crack length extends beyond the notch field and ΔK can be estimated using an effective crack given by the notch depth plus the physical crack depth ($b + a$) subjected to the remote stress.

Between the above two limiting forms of threshold behavior, a third type of threshold behavior can occur – the "worst-case notch"

phenomenon. This phenomenon is characterized by the occurrence of a local maximum in the $\Delta S_{th}(a)$ curve, as indicated by the open symbols in Fig. 20. This local maximum occurs at a crack depth $a^* = (ba_o)^{1/2}$ and at a limiting threshold stress ΔS_{th}^* given by [74]

$$\Delta S_{th}^* = \frac{\Delta K_{th}(R)}{F\sqrt{\pi}(\sqrt{b}+\sqrt{a_o})} \tag{19}$$

For sharp notches, this local maximum is of particular significance since it defines the conditions under which cracks will either arrest ($\Delta S_{th} < \Delta S_{th}^*$) or continue to propagate to failure ($\Delta S_{th} > \Delta S_{th}^*$). This crack arrest/propagation behavior is the direct consequence of the crack-size dependent threshold.

For crack initiation at a pore with a local radius, ρ, and stress contraction factor, k_t, the cycle to crack initiation is given by [29]

$$\left[k_t \Delta S \left(1 - \frac{r^*}{\rho} \right) - \Delta \sigma_e \right] N_i^\alpha = \zeta \tag{20}$$

where r^* represents the distance ahead of the pore dominated by crack initiation. The r^*/ρ is about 0.4 at $k_t = 2$ and decreases to about 0.04 at $k_t = 5$. Eq. (20) indicates that S–N_f curves with dual fatigue limits are feasible for cast alloys that contain pores with $k_t > k_t^*$, but only a single fatigue limit would be observed in cast alloys that contains pore with $k_t < k_t^*$, as depicted in Fig. 20 for steels with $k_t^* \approx 3$.

One important finding of the worst-case notch that is the existence of no-growth regime when the stress concentration factor, k_t, exceeds a critical value ($k_t > k_t^*$) and its absence of at $k_t < k_t^*$. This information has been utilized to construct a Kitagawa diagram for materials containing pores with a sharp pore-tip ($k_t > k_t^*$) shown in Fig. 21, using the analogy between pores and notches with equivalent depth and radius of curvature. In Fig. 21, stress range, $\Delta\sigma$, is plotted again the crack length, which is the sum of the half-length, a_p, of the pore and the actual crack length, a, emanating from the pore-tip. The fatigue limit dominated by crack initiation as shown by the horizontal line at $\Delta\sigma = \Delta\sigma_e/k_t$, where $\Delta\sigma_e$ is the fatigue limit of the pore-free material. This corresponds to the horizontal fatigue limit in the traditional Kitagawa diagram. The slanted solid line in Fig. 21 corresponds to the failure boundary dominated by the large-crack FCG threshold, as in the traditional Kitagawa diagram [62]. The stress concentration by a notch or pore creates a fatigue failure regime that is dominated by non-propagation of small cracks. This region is bounded by the horizontal solid line at

$\Delta\sigma_s = \Delta\sigma_e/k_t^*$ and $\Delta\sigma = \Delta\sigma_e/k_t$. The transition points a_1 and a_2 are analogous to a_o and are given by

$$a_1 = \frac{1}{\pi} \left(\frac{k_t^* \Delta K_{th}^{LC}}{F \Delta\sigma_e} \right)^2 \tag{21}$$

and

$$a_2 = \frac{1}{\pi} \left(\frac{k_t \Delta K_{th}^{LC}}{F \Delta\sigma_e} \right)^2 \tag{22}$$

with $a_2 > a_1$ since $k_t > k_t^*$. Three initial pore size distributions are also depicted in Fig. 21. For the pore size distribution labeled Type A, $a_p < a_1$. In Type B, the mean a_p is about a_1 so that some pores are larger than a_1 and some are smaller than a_1. In contrast, $a_p > a_1$ for the pore distribution labeled Type C. Type A pore distribution would lead to an S–N_f curve with double fatigue limits similar to those depicted in Fig. 1a. The short-life apparent fatigue limit is caused by the arrest of small cracks within the pore-tip stress field. The long-life fatigue limit is one that is dominated by crack initiation and growth of small cracks to failure. On the other hand, Type B pore distribution would lead to an S–N curve similar to the one depicted in Fig. 1b. In this case, the stress gradient ahead of the sharp pore-tip with $k_t > k_t^*$ is sufficiently steep that the local ΔK at the crack tip can fall below the growth threshold such that a fatigue crack can become arrested after initiation. The non-propagating microcracks can increase in size not by growth, but by coalescing with adjacent microcracks when additional new microcracks are nucleated. Thus, the apparent fatigue limit is the result of crack coalescence by non-propagating or slow-propagating small cracks. For Type C, the S–N_f curve would be entirely dominated by the growth of large-cracks. Since the limiting stress range is controlled by ΔK_{th}, the resulting S–N curve would be without a fatigue limit. Thus, three types of S–N_f curves with different shapes with no or multiple fatigue limits are feasible in cast alloys with notch-like pores, depending on the pore shape and the pore size distribution.

4. Crack initiation at inclusions or particles

Fatigue crack initiation at inclusion or hard particles is quite common in steels [16,17,77–83], Al alloys and casting [67,71], and Ni-based alloys [12,15,84–93]. For titanium alloys, fatigue crack initiation at hard particles is rare, but fatigue crack initiation at hard alpha was the cause of the failure of a Ti rotor [94]. In both wrought and cast Al alloys, intermetallic particles are brittle, which fracture under monotonic or cyclic loading, and can form a microcrack [67,71]. The particle crack can subsequently initiate a fatigue crack in the matrix and propagate to failure.

The influence of inclusion size, spacing, and clustering on fatigue crack incubation in cast Al alloys has been investigated by Fan et al. [72] and McDowell el al. [95] using an FEM-based micromechanical approach. Using inclusions of several sizes, spacing values, and numbers, these investigators [72,95] computed the local strain amplitudes in the inclusion-containing specimen subject to various stress amplitudes. The local strain amplitudes were used to estimate the cycles to crack incubation using either the Coffin–Manson equation [30,31] or the Fatemi–Socie critical plane criterion [73]. In general, larger inclusions concentrate higher plastic strain and lead to a lower fatigue crack incubation life [72]. Similarly, the local plastic strain increases with increasing numbers of inclusion and leads to lower incubation life [72]. The maximum plastic strain range is highest when the inclusion spacing is on the order of the inclusion size. Local strain concentrations at cracked and debonded inclusions have also been analyzed for martensitic gear steels via this local strain approach [96].
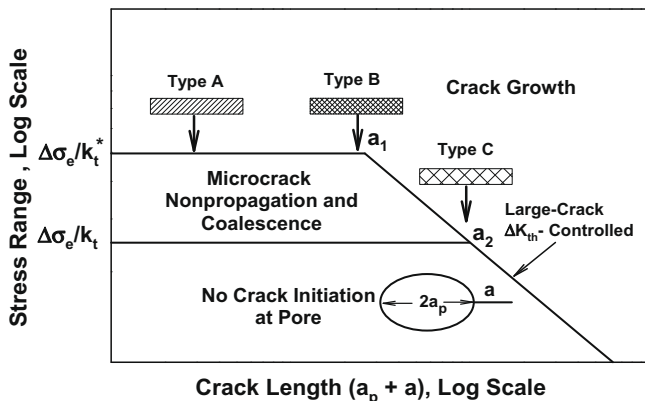
Fig. 21. Kitagawa diagram for materials containing pores with notch-like features. The schematic depicts a crack initiation-free region, a microcrack non-propagation and coalescence region, and a crack growth region. Three different pore distributions are superimposed to illustrate the role of pore size on the shape of the S–N_f curve. Type A pores lead to a S–N_f curve with double fatigue limits. Type B pores lead to a S–N_f curve with a fatigue limit, and Type C pores result in no fatigue limit in the S–N_f curve.

In Ni-based disk alloys, fatigue crack initiation sites include ceramic inclusions, pores, and planar slipbands. Gell and Leverant [12] reported fatigue crack initiation at non-metallic inclusions such as carbides and pores in directionally-solidified Mar-M200. Stage I and Stage II initiation also occurs in wrought and cast Ni-based superalloys. The controlling fatigue mechanisms vary with temperature, frequency, environment, and slip morphology. Major defects in PM Ni-based alloys include discrete chucky ceramic particles (Type I), ceramic agglomerates (Type II), reactive agglomerates forming prior particle boundaries, and pores [85,86]. Hyzak and Bernstein [84] reported fatigue crack initiation from pores, inclusions, and crystallographic facets in two powder-metallurgy Ni-based alloys. There was a tendency for surface initiation at high strain ranges but interior initiation at lower strain ranges. Stage I initiation is dominant at room temperature, while initiation at pores and inclusion dominates at elevated temperatures. Similar observations were reported for PM Ni-based alloys such Rene 88, Rene 95, and advanced PM Ni-based alloys using seeded inclusions [15,85–93]. These studies showed conclusively that the fatigue life of PM Ni-based alloys is significantly affected by the inclusion size distribution, the pore size distribution, and the grain size distribution. For a given defect size or area, the LCF life is lower for surface initiation compared to interior initiation. Under certain conditions, the fatigue life of PM alloys with non-metallic inclusions can be dominated by fatigue crack growth to failure [15,92,93] and be enhanced by interior initiation at least partly due to slower FCG kinetics in vacuum compared to air [12,90]. Extensive work at AFRL has shown that in many Ni-based disk alloys, substantial fatigue life variations occur in Ni-based disks alloys where fatigue cracks initiated from non-metallic inclusions located at either the specimen surfaces or in the interior region [15,92,93]. Specimens that were dominated by small-crack growth resulted in low fatigue lives in the 10^4–10^5 range, while specimens that dominated by crack initiation led to longer lives in the 10^7–10^8 range. The fatigue life correlated with neither the inclusion size nor the location. The large discrepancy in the fatigue life indicated substantial variations in the crack initiation life, ranging from negligible to in the HCF regime.

Ceramic or non-metallic inclusions that have different coefficients of thermal expansion than the matrix may induce residual stresses in the matrix where they reside and in the inclusions themselves during processing or subsequent heat-treatments involving temperature changes. These residual stresses, known as tessellated or textural stresses [97], are known to occur around some inclusions such as alumina, TiN, and other oxide particles in steels [97]. For both spherical and cylindrical particles, these inclusions lead to compressive residual stresses in the inclusions (circumferential direction), but tensile residual stresses (also in the circumferential direction) in the ferrite matrix, as shown in Fig. 22a [97]. For Ti or Ti-alloy matrix with a hard alpha particle in the circumferential direction, the residual stresses are typically compressive in the hard alpha particle but are tensile in the matrix, as shown in Fig. 22b [98]. In contrast, little information is available in the open literature on the textural stresses around inclusions in Ni-based alloys.

Fatigue crack initiation at particles is more complex since it can affect the ζ term in Eq. (12) when the particles crack or serve as the crack initiation site. As shown in an earlier publication [35], the fatigue life coefficient, ζ, for crack initiation at hard particles is given by

$$\zeta = \left[\frac{8(\mu + \mu')}{\lambda \mu'}\right]^{1/2} \left[\frac{M\mu h^2}{d(h+d)}\right] \left[\frac{c}{\xi}\right]^{1/2} \qquad (23)$$

where μ' is the shear modulus and ζ is the size of the particles. Furthermore, the presence of particles in the microstructure can induce
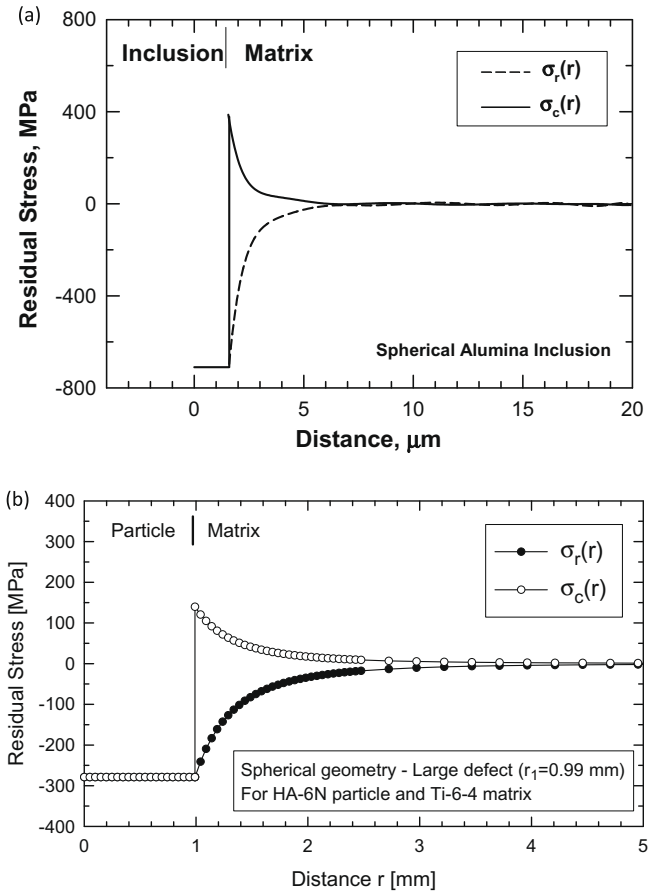

Fig. 22. (a) Residual stress in steel in the Al$_2$O$_3$ inclusions (Brooksbank and Andrews [97]) and (b) residual stress profile as a function of distance for an HA particle with 6%N embedded in a Ti–6Al–4V matrix and assuming a spherically shaped particle. $\sigma_r(r)$ is the radial stress, while $\sigma_c(r)$ is the circumferential stress at a distance, r, from the center of the hard alpha particle (Laz et al. [98]).

residual stresses in the particles and the matrix during themomechanical processing with temperature variations and subsequent heat treatments when there is a difference in the coefficients of thermal expansion (CTE), as in the case for hard alpha particles in a Ti-alloy matrix. Typically, the residual stresses in the hard particles are compressive, while the corresponding residual stresses are tensile in the Ti-alloy matrix and in steels. While the presence of hard particles may reduce the ζ term and promote crack initiation, the compressive residual stresses induced by the difference in the CTE may delay crack initiation, creating two opposite and competing effects for crack initiation at the hard alpha particles. The compressive residual stresses can lead to positive deviation from the Goodman line, leading to non-linear σ_a–σ_m relation that is best described in terms of the Gerber parabola [99]. When a tensile residual stress, σ_{rs}, exists in the Ti-alloy matrix, Eq. (13) is applicable to this situation as residual stress can be considered as one form of microstructural constraint stress. Replacing σ_{mc} in Eq. (13) with σ_{rs} leads one to [36]

$$\sigma_a = \left[\frac{\zeta}{2} N_f^{-\alpha} + Mk\right] \left[1 - \frac{\sigma_m}{\sigma_{UTS}} - \frac{\sigma_{rs}}{\sigma_{UTS}}\right] \qquad (24)$$

which indicates that a tensile residual stress would assist crack initiation in the matrix in a manner similar to the microstructurally-induced constraint stress induced by primary α grains. In particular, a tensile residual stress in the matrix would alter the fatigue life dependence on means stress from a linear relation to the bilinear relations depicted in Fig. 23a. On this basis, the effects of soft grains

and hard particles on high-cycle fatigue life can be similar. In both cases, the local mean stress and the corresponding local stress ratio, R, are increased at interior soft grains or at the matrices adjacent to hard particles to lower the stress amplitude for a given fatigue life such that the modified Goodman relation would over-predict the fatigue strength. In Ti-alloys and steels, the hard particles examined (e.g., TiN or TiN_x) typically lead to compressive residual stresses in the particles that delay particle fracture but tensile residual stresses in the matrix that shift fatigue crack initiation at a higher mean stress. Despite the increase in mean stress, the crack initiation life can be increased by virtue of a higher Taylor factor and uniformity of slip in the interior grains.

According to Eqs. (21) and (22), a longer fatigue life can be expected by virtue of increased M and ζ values when slip becomes more uniform in the interior region. The ζ parameter is increased when the shear modulus is higher and the size of the inclusion is smaller than the counterpart of the matrix. The fatigue limit can be reduced in the UHCF region by the tensile residual stresses in the matrix. Alternately, the fatigue limit can be reduced in the UHCF regime when the inclusion size exceeds that pile-up length or grain size in the interior region. The changes in the microstructural parameter would cause a shift of the S–N_f to the longer life and lower the fatigue limit, as depicted in Fig. 23b.

In gigacycle fatigue of steels, fatigue crack initiation sites are inclusions in the interior region, which failure surfaces often give the appearance of a fish-eye [16,17,77–79]. Fig. 24 illustrates the fracture surface with a fish-eye [79]. The crack starts from an inclusion embedded in an optically dark region, which is divided into an
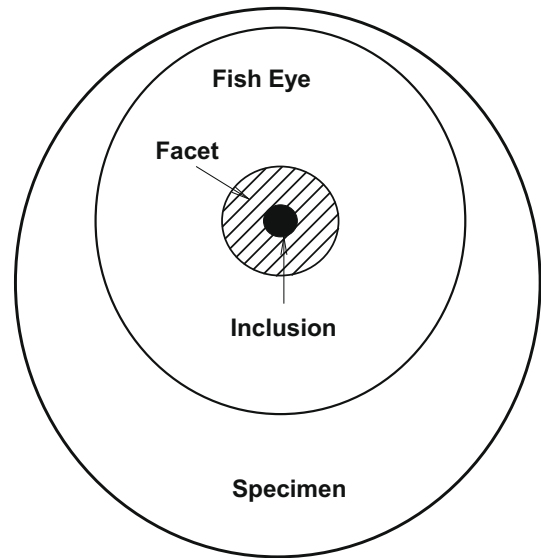

Fig. 24. Schematic depiction of fracture surface with fish-eye [79].

Fig. 23. Schematics show the effect of a CTE-induced tensile residual stress in the matrix adjacent to an inclusion on the fatigue life: (a) effect on σ_a–σ_m plot and (b) effect of S–N_f curve.

inner facet region and an outer rough region. The S–N_f curves of a bearing steel are presented in Fig. 25 [77,79]. Like many other steels [80–83], this bearing steel exhibited surface-initiated and interior-initiated fatigue fracture. The origins of surface cracks were inclusions and slipband facets. For internal fatigue, the crack originated from a non-metallic inclusion at the center of the fish-eye. The transition from surface to internal fatigue resulted in a shift of the S–N_f curves to longer fatigue cycles. This transition can be understood on the basis of textural stresses near the inclusions, which are compressive in the inclusions and tensile in the matrix for most types of inclusions in steels. Instead of crack initiation, the observed shift of S–N_f curve in steels has been explained also by Tanaka and Akiniwa [79] on the basis of a fatigue crack growth theory and hydrogen embrittlement in the interior region.

The Kitagawa diagram for materials containing inclusions with tensile residual stresses in the adjacent matrix is shown schematically in Fig. 26, which plots the stress range against the crack length. As shown in the insert, the crack length is the sum of the half-length, a_p, of the inclusion and the actual crack length, a, emanating from the inclusion. The fatigue limit dominated by crack ini-
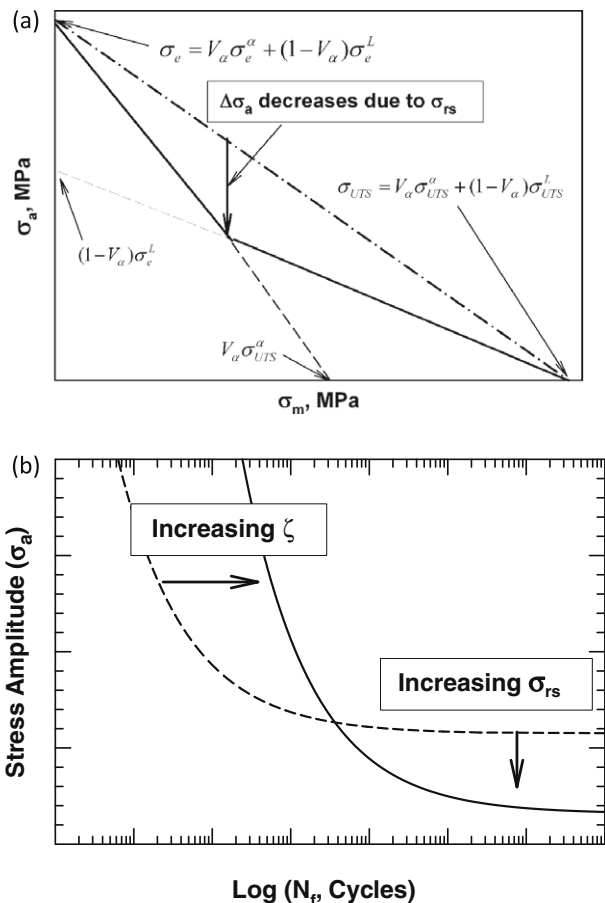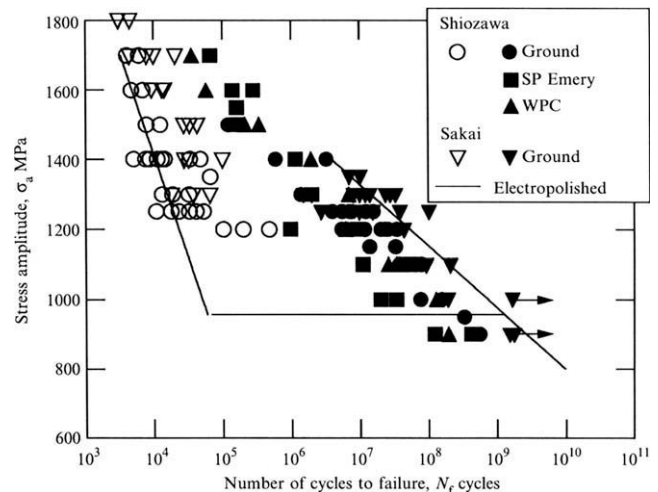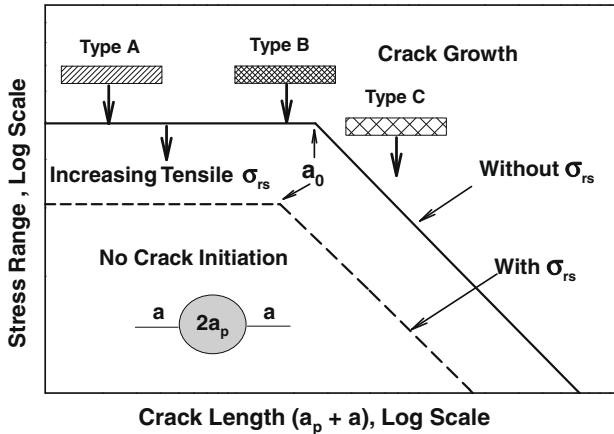

Fig. 25. S–N_f curves of a bearing steel with electropolished, ground and peened surfaces. From Tanaka and Akiniwa [79].

Fig. 26. Kitagawa diagram for materials containing inclusions that induce residual tensile stresses in the matrix. The schematic depicts a crack initiation-free region and a crack growth region as in a traditional Kitagwa diagram. The limiting stresses of these two failure boundaries are both decreased by increasing residual tensile stresses. Three different particle distributions are superimposed to illustrate the role of inclusion size on the shape of the $S-N_f$ curve. Type A inclusions lead to an $S-N_f$ curve with double fatigue limits. Type B inclusions lead to an $S-N_f$ curve with a fatigue limit, and Type C inclusions result in no fatigue limit in the $S-N_f$ curve.

tiation is shown by the horizontal line at $\Delta\sigma_e$ and the slanted solid line in Fig. 26 corresponds to the failure boundary dominated by the large-crack FCG threshold, as in the traditional Kitagawa diagram [62]. The higher limiting stresses correspond to those for surface initiation. For interior initiation at an inclusion, both limiting stresses are decreased due to the presence of CTE-induced tensile residual stresses in the matrix, as shown in Fig. 23b. To explain the various shapes of the $S-N_f$ curve, three inclusion size distributions are also depicted in Fig. 26, with the arrow indicating decreasing stresses at constant a constant length. For the inclusion size distribution labeled Type A, $a_p < a_0$. Type A inclusion size distribution would lead to an $S-N_f$ curve with double fatigue limits similar to those depicted in Fig. 1a, when surface initiation is replaced by interior initiation in the UHCF regime. The short-life apparent fatigue limit is the result of crack initiation and the growth of small cracks from an inclusion at an interior site. The long-life fatigue limit is one that is dominated by crack initiation and growth of small cracks to failure. In Type B, the mean a_p is about a_0 so that some inclusions are larger than a_0 and some are smaller. Type B inclusion size distribution would lead to an $S-N_f$ curve similar to the one depicted in Fig. 1b, which is dominated mostly by crack initiation and the growth of small cracks. In contrast, $a_p > a_0$ for the inclusion size distribution labeled Type C. For Type C, the $S-N$ curve would be entirely dominated by the growth of large-cracks. Since the limiting stress range is controlled by the large-crack ΔK_{th}, the resulting $S-N$ curve would be without a fatigue limit. Thus, three types of $S-N_f$ curves with different shapes with no or multiple fatigue limits are feasible in PM alloys, depending on the inclusion size distribution, a_0, and the residual tensile stresses in the matrix.

For a Ni-based PM disk alloy (N18), Bathias and Paris [90] reported the occurrence of competing mechanisms of crack initiation at pores and inclusions in unseeded (standard) and seeded, polished specimens. These $S-N_f$ data are presented in compared in Fig. 27, which shows the failure stress decreases gradually with increasing fatigue cycles without an obvious endurance limit. In the UHCF regime, fatigue crack initiation starts in the interior region from a defect. The initiation site is mainly a pore for the unseeded (standard) material, but a ceramic (alumina) inclusion for the seeded material. For both cases, the fatigue life of N18 in the UHCF is dictated by the formation of persistent slipbands and crack initiation from the defect, and not by the growth of small cracks.
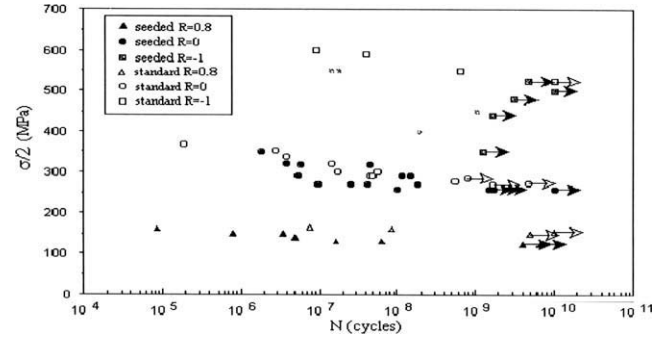
Fig. 27. Comparison of $S-N_f$ curves of PM Ni-alloy (N18) with and with seeded inclusions at various R ratios. Fatigue crack initiated at pores in unseeded specimens but at inclusions in seeded specimens. From Bathias and Paris [90].

Other fatigue studies of PM Ni-based superalloys appear to report inclusion effects on crack initiation and fatigue life that are different from those observed by Bathias and Paris on N18 [90]. A number of studies [15,90,93] reported that hard particles formed cracks early and the fatigue life of these PM alloys were dominated by the growth of small cracks to become large-cracks and failed when a critical crack length was reached [15]. These observations were made at stress amplitudes that led to fatigue life in the 10^7 and 10^8 cycle range in specimens dominated by crack initiation at slipbands or crystallographic facets, as shown in Fig. 28. The consequence is a large variation in fatigue life, which is separated into a short life distribution and a longer life distribution. The former is dominated by fatigue crack growth, while the latter is dominated by fatigue crack initiation. The apparent lack of crack initiation in hard particles associated the short life distribution may be rationalized on the basis that these hard particles might contain preexisting cracks or tensile residual stresses that cause easy crack formation in the particles. The corresponding compressive stresses in the matrix may be sufficiently low that fatigue crack growth is not impeded. Under this circumstance, a fatigue crack can initiate at a negligible crack initiation life and propagate to failure at a relative short total life. Obviously, this is only one of the many possible scenarios for easy crack initiation in PM alloys with multiple types and size of hard particles and potential crack initiation sites. Like crack initiation at pores, crack initiation and growth at inclusions appears to lead to very different $S-N_f$ curves,
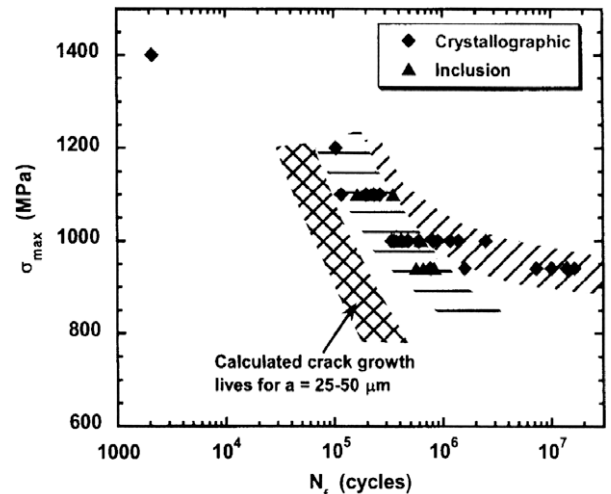
Fig. 28. The role of crack growth in the lifetimes of inclusion-initiated and slipband-initiated fatigue fracture in Rene 88 DT. From Caton et al. [15].

depending on inclusion type, size, and distribution, as well as the sense of textural stresses, if any, resulted from CTE interactions between the matrix and the inclusions. Many aspects of the fatigue process at inclusions are not well understood and more research is required to develop a better understanding and more accurate life-prediction methods.

Besides crack initiation at hard particles, there have also been substantial amounts of efforts devoted to developing accurate constitutive models based on crystal plasticity theories for Ni-based superalloys [100–102]. These models address the effects of grain size [100,101] as well as the primary, secondary, and tertiary γ' precipitates [101–103] on the cyclic stress–strain response by considering their respective particle size distributions. The constitutive models are then utilized to compute a number of fatigue index parameters (FIPs) for a representative volume element (RVE) of the microstructure of interest [103]. These FIPs, which are intended to represent the driving force for crack incubation in the RVE, are defined in terms of the cumulative plastic strain [100], the Fatemi–Socie critical plane parameter [73], or the cyclic plastic shear strain amplitude [103]. Manonukul and Dunne [100] showed that the a polycrystal plasticity FEM model combined with a fatigue crack initiation criterion based on a critical cumulative shear strain correctly predicts the standard Goodman correlation [37] in HCF, and the Coffin–Manson correlation [30,31] in LCF.

5. Crack initiation at machined surfaces

Crack initiation from the machined surfaces of a bore hole has been identified as the origin of the fatigue crack that propagated during service and caused of the failure of a Ti hub in a commercial aircraft [104]. The fatigue crack originated from a re-crystallized α grain situated on the machined surface. Fatigue cracks initiated at the machined surfaces and their subsequent propagation to failure was also identified as the cause of the fatigue fracture of a structural component in a military aircraft [105]. For fatigue cracks initiated from machined surfaces, the initiation life is often, rightly or wrongly, considered small and the fatigue life is expected to be controlled by the crack growth life. In an earlier study, Taylor and Clancy [11] showed that for some machined surfaces, fatigue life is dominated by crack initiation and small-crack growth, as shown in Fig. 29, which presents a Kitagawa plot for several machined surfaces with varying degrees of surface roughness. Most, if not all, of the data points lie on or near the horizontal fatigue lim-
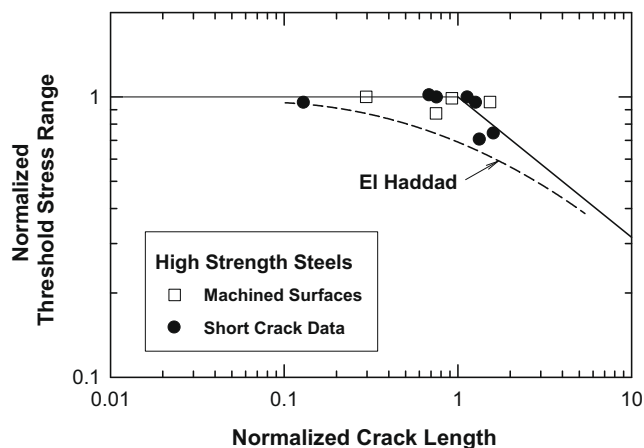
Fig. 29. Normalized Kitagawa diagram with fatigue data from machined surface with various surface roughness (polished, ground, or milled) compared to short crack data in high strength steels. The fatigue life of the machined surfaces is controlled by crack initiation and the growth of small cracks, but not large-cracks. From Taylor and Clancy [11].

it, indicating dominance by crack initiation and probably small-crack growth. Along the same vein, several investigators treated fatigue crack initiation from machined surfaces by approximating the surface trough as a micro-notch with a characteristic width, depth, and root radius, accompanied by an elastic stress concentration factor and a notch sensitivity factor [106–109]. Thus, fatigue of machined surfaces has been treated in terms of conventional notch fatigue strength analysis by expressing the k_t factor as a function of the roughness of the machine surfaces [106]. Moreover, it is not uncommon for machined surfaces of engineering components to be peened to induce compressive surface stresses for the purpose of delaying fatigue crack initiation, fatigue crack growth, or both. Machined bore holes in aero-engines are shot-peened [110] but more advanced techniques such as laser-shock peening or low-plasticity burnishing have been developed [111,112]. Currently, there are no fatigue life data of machined surfaces in the gigacycle fatigue regime. Thus, it remains unknown whether or not a transition from surface initiation to interior initiation would occur in components with machined surfaces.

Fatigued surfaces are often rough due to the presence of slip extrusions formed on metal surfaces subjected to cyclic loading [3–8]. The roughened surfaces [3,6] can lead to fatigue crack initiation, including machined surfaces [11,113]. For structural components, the machined surfaces may be sufficiently rough to obscure the detection of surface roughness due to persistent slipbands or extrusions. Buckner et al. [114] recently obtained surface roughness measurements on machined surfaces of Waspaloy with and without fatigue. Significant differences were observed in the bidirectional reflectance distribution (BRDF) signal levels of the pristine and fatigued machined surfaces. The challenge is how to relate the BRDF signals, which is a measure of surface roughness, to the onset of fatigue crack initiation.

According to Chan et al. [29], the cumulative roughness, R_a, of a surface grain can be taken as the cyclic displacements accumulated on the grain surface over the fatigue cycles and it is given by

$$R_a = \frac{C_1 M}{\Delta \varepsilon_p} \left(\frac{h}{w} \right) \Delta \delta \qquad (25)$$

where $\Delta \delta$ is the cycle slip displacement; $\Delta \varepsilon_p$ is the cyclic plastic strain range; h is the slipband width and w is the slipband spacing; C_1 is a constant. During cyclic loading, the h/w ratio increases with increasing fatigue cycles and R_a is increases with increasing fatigue cycles. The ratio of the slipband-width-to-spacing increases with increasing fatigue cycles at a diminishing rate and the ratio appears to saturate to about ~0.5–1 at fatigue cycles greater than 10^4 cycles, and fatigue crack initiation occurs when the slipband-width-to-spacing ratio increases to a value of ~0.5–1 for Ni200. Thus, the evolution of roughness of a fatigued surface may potentially be used as a damage precursor or indicator to prognosticate fatigue crack initiation from a surface, as demonstrated by Buckner et al. [114] on machined surfaces of Waspaloy, as shown in Fig. 30. A region of high surface roughness may indicate a region where cyclic deformation and slipband formations are prevalent. With continued cyclic deformation, slip can concentrate further and become localized into a fatigue crack when the slipband-width-to-spacing ratio approaches about 0.5–1. In a recent study, Brinckmann and Van der Giessen [115] presented computational results that simulated the evolution of slip steps on a fatigue surface using dislocation dynamics and a cohesive zone approach. The computation was carried for cyclic tension and compression of a single plastically deformed grain at a free surface surrounded by elastic grains. A normalized separation parameter defined based on the cycle-to-cycle maximum cohesive opening was computed and used as a measure of surface roughness during cyclic deformation [115]. The computational results indicated that the value of the normalized separation
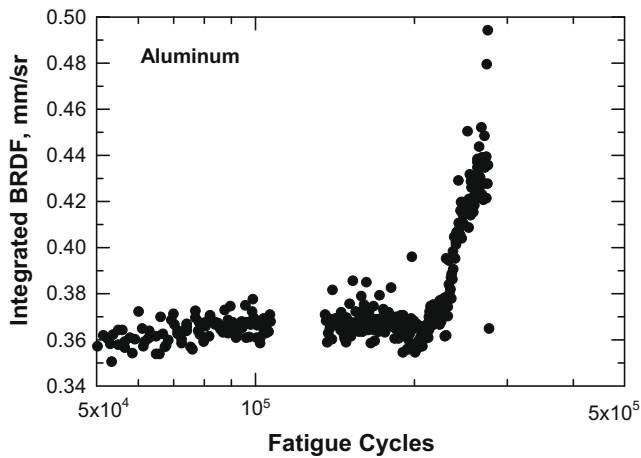
Fig. 30. Line-integrated BDRF as a function of fatigue cycle during LCF of aluminum. From Buckner et al. [114].

parameter increases slowly with increasing fatigue cycle, but the growth rate increases rapidly at larger fatigue cycles. The shape of the predicted surface roughness versus fatigue cycle curve is qualitatively similar to that of the line-integrated BRDF data shown in Fig. 30. Taken together, both the experimental and numerical results in the literature support the notion that a region with a high surface roughness may indicate a likely site for fatigue crack initiation. It should also be noted that whether or not fatigue-induced surface roughness can be detected obviously depends on the initial roughness of the surface conditions. In particular, fatigue-induced surface roughness must exceed the initial surface roughness in order for surface roughness to be a viable fatigue prognostic indicator. Recent work by Buckner et al. [114] indicated that fatigue-induced surface roughness could be ascertained even from machined surfaces because of significant differences between the BRDF response of the fatigued and unfatigued machined surfaces.

On the other hand, a transition from surface initiation to interior initiation is likely to make fatigue crack detection a more difficult task as many surface detection techniques are rendered inappropriate and ineffective. Bathias and Paris [90] recently pointed out that it seems difficult to apply a damage tolerance approach to predict the fatigue life of a structural component such as PM Ni-alloy disk when interior initiation dominates in the gigacycle fatigue regime because of the difficulties in detecting internal crack initiation and growth using traditional NDE techniques.

6. Prospects and challenges for future development

This review identified more than four fatigue crack initiation mechanisms that may occur concurrently and compete for dominance in a given microstructure. Considerable progress has made to characterize the microstructural features that promote crack nucleation and fatigue life variability. There is, however, a lack of knowledge on the attributes, microstructural or otherwise, that result in the formation of the worse-case crack, one that produces the lowest total fatigue life. Since many microstructural parameters affect the crack nucleation process, the worse-case crack may not be dominated by one or two microstructural parameters in a long list of variables such as grain size, texture, slip planarity, pores, and among other, inclusions, but is related to interactions of most, if not all, of these microstructural variables in a manner that may or may not be obvious.

Identifying the relevant microstructural variables which interactions contribute to the worst-case crack is a challenge, but could be accomplished through systematic experimentation and analyzing the results through multivariate analyses. While the interaction effects of a group of variables can be discerned using a multivariate analysis, the author prefers and advocates the use of in situ fatigue experimentation to observe directly the controlling fatigue mechanisms as pioneered by Davidson and Lankford [116]. By coupling the in situ observations with micromechanical models containing explicit microstructural variables as illustrated in this review paper, the microstructural attributes of the worse-case fatigue crack in a given microstructure may be identified unambiguously in many, though not all, situations. Substantial 3D measurements have been obtained for a number of fatigued materials. This valuable information may be utilized by 3D microstructural models for advancing the current understanding of the interaction effects of microstructural variables and for quantitative predictions of fatigue life variability. Future work is required to combine 3D microstructural data with appropriate modeling to make realistic and quantitative life-prediction for extension of component lives.

One of the unresolved issues identified in this review is the role of fatigue crack growth in ultra-high-cycle fatigue that produces fish-eye fracture appearance. One view is that it is dominated by crack growth, while others believe that it is controlled by crack nucleation. Since crack nucleation and growth occurs internally, detecting the onset of crack nucleation and the subsequent growth of the small cracks is a challenge and requires the development of new techniques for measuring internal cracks at small crack sizes. Another challenge is an accurate determination of any processing-related residual stresses at the crack nucleation site and the evolution of these residual stresses with fatigue cycles.

Another area where future development is needed is a better understanding of the evolution of surface roughness and the critical conditions that lead to the onset of crack formation. New characterization and modeling techniques have improved the current understanding of the origins of surface roughness and its relationship with fatigue damage and crack nucleation, but further developments are still needed to establish direct relationships between optical reflectance measurements, surface roughness, and fatigue crack nucleation. These new developments are needed to provide the scientific basis to advance Laser-based optical reflectance technology into a practical prognostic tool for assessing the state of fatigue damage and for predicting the remaining life of structural components.

7. Concluding remarks

This overview summarizes the current understanding of the roles of microstructure in fatigue crack initiation in pure metals and structural alloys. Microstructural parameters that influence fatigue crack initiation at slipbands, grain boundaries, pores, inclusions, and machined surfaces are identified and utilized to explain the transition from surface initiation to interior initiation, the formation of multiple fatigue limits in some alloys and their absence in other materials. The conclusions reached as the result of this review are as follows:

1. Microstructure can produce internal textural stresses that can alter the stress–life relations in multiphase alloys by producing double fatigue limits. These textural stresses include microstructure-induced plastic constraint stresses resulting for plastic interactions among soft and hard grain in the microstructure or CTE-induced thermal stresses resulting from thermo-mechanical interactions between matrix grains and non-metallic inclusions.
2. For materials exhibiting double fatigue limits in the $S–N_f$ curve, the higher stress limit is controlled by the growth of small cracks and the lower stress limit is controlled by crack initiation.

3. Fatigue crack initiation at defects such as pores, inclusions, and machined marks can lead to S–N_f curves with no, one, or double fatigue limits, depending on the defect (pore, inclusion, or machine mark) size distribution.

4. A Kitagawa diagram is a useful tool for distinguishing changes in the controlling fatigue mechanism by crack initiation, crack coalescence, small-crack growth, and large-crack growth.

5. Coalescence of non-propagating microcracks to form a larger crack by continuous crack nucleation appears to be the predominant fatigue mechanism responsible for the occurrence of an apparent fatigue limit in a double-stage S–N_f curve.

6. Competition between initiation-controlled and growth-controlled fatigue mechanisms results in large variations in fatigue life.

7. Understanding of fatigue initiation and growth at internal sites is far from complete and methodology for predicting its occurrence is still in its infancy.

References

[1] Davidson DL, Chan KS, Hudak Jr SJ, McClung RC. Small fatigue cracks. In: Ritchie RO, Murakami Y, editors. Comprehensive structural integrity. Cyclic loading and fatigue, vol. 4. Oxford, UK: Elsevier; 2003. p. 129.
[2] Miller KJ. The behaviour of short fatigue cracks and their initiation part II – general summary. Fatigue Fract Eng Mater Struct 1987;10:93–113.
[3] Wood WA. Fatigue in aircraft structures. New York: Academic Press; 1956.
[4] Fine ME, Ritchie RO. Fatigue-crack initiation and near-threshold crack growth. In: Meshii M, editor. Fatigue and microstructure. Metals Park (OH): ASM; 1978. p. 245–78.
[5] Laird C. Mechanisms and theories of fatigue. In: Meshii M, editor. Fatigue and microstructure. Metals Park (OH): ASM; 1978. p. 149–203.
[6] Klesnil M, Luksa, P. Fatigue of metallic materials. New York (NY): Elsevier; 1980. p. 57–80 [chapter 3].
[7] Mughrabi H. Rev Phys Appl 1988;23:367–79.
[8] Mughrabi H. In: Chan KS, Liaw PK, Bellows RS, Zogas T, Soboyejo WO, editors. Fatigue: David L. Davidson symposium. Warrendale (PA): TMS; 2002. p. 3–15.
[9] Davidson DL, Chan KS. Crystallography of fatigue crack initiation in Astrology at ambient temperature. Acta Metall 1989;37(4):1089–97.
[10] Suresh S. Fatigue of materials. 2nd ed. Cambridge University Press; 1998. p. 132–64.
[11] Taylor D, Clancy OM. The fatigue performance of machined surfaces. Fatigue Fract Eng Mater Struct 1991;14:329–36.
[12] Gell M, Leverant GR. Mechanisms of high-temperature fatigue. In: Fatigue at elevated temperatures, ASTM STP 520. American Society for Testing and Mater; 1973. p. 37–67.
[13] Jha SK, Larsen JM, Rosenberger AH, Hartman GA. Dual fatigue failure models in Ti–6Al–2Sn–4Zr–6Mo and consequences on probabilistic life prediction. Scripta Mater 2003;48:1637–42.
[14] Ravi Chandran KS, Jha SK. Duality of the S–N fatigue curve caused by competing failure modes in a titanium alloy and the role of Poisson defect statistics. Acta Mater 2005;53:1867–81.
[15] Caton MJ, Jha SK, Rosenberger AH, Larsen JM. Divergence of mechanisms and the effect on the fatigue life variability of Rene 88 DT. In: Green KA, Pollock TM, Harada H, Howson TE, Reed RC, Schirra JJ, et al., editors. Superalloys 2004. TMS (The Minerals, Metals and Materials Society); 2004. p. 305–14.
[16] Nishijima S, Kanazawa K. Stepwise S–N curve and fish-eye failure in gigacycle fatigue. Fatigue Fract Eng Mater Struct 1999;22:601–7.
[17] Murakami Y, Nomoto T, Ueda T. Factors influencing the mechanism of superlong fatigue failure in steels. Fatigue Fract Eng Mater Struct 1999;22:581–90.
[18] Mughrabi H. On 'multi-stage' fatigue life diagrams and the relevant life-controlling mechanisms in ultrahigh-cycle fatigue. Fatigue Fract Eng Mater Struct 2002;25:755–64.
[19] Morrison DJ, Chopra V. Mater Sci Eng 1994;A177:29–42.
[20] Buque C. Int J Fatigue 2001;23:459–66.
[21] Buque C, Bretschneider J, Schwab A, Holste C. Mater Sci Eng 2001;A300:254–62.
[22] El-Madhoun Y, Mohamed A, Bassim MN. Mater Sci Eng 2004;A386:140–7.
[23] Harvey SE, Marsh PG, Gerberich WW. Acta Metall Mater 1994;42:3493–502.
[24] Man J, Obrtlik K, Blochwitz C, Polak J. Acta Mater 2002;50:3767–80.
[25] Polak J, Man J, Obrtlik K. Int J Fatigue 2003;25:1027–36.
[26] Polak J, Man J, Vystavel T, Petrenec M. Mater Sci Eng A 2009;A517:204–11.
[27] Saxena A, Antolovich SD. Metall Trans A 1975;6A:1809–28.
[28] Depres C, Robertson CF, Fivel MC. Mater Sci Eng 2004;A387–A389:288–91.
[29] Chan KS, Tian JW, Yang B, Liaw PK. Evolution of slip morphology and fatigue crack initiation in surface grains of Ni200. Metall Mater Trans A 2009;40A:2545–56.
[30] Coffin Jr LF. Trans ASME 1954;76:931–50.
[31] Manson SS, Hirschberg MH. Fatigue: an inter-disciplinary approach. Syracuse (NY): Syracuse University Press; 1964. p. 133–78.
[32] Tanaka K, Mura T. A dislocation model for fatigue crack initiation. ASME J Appl Mech 1981;48:97–103.
[33] Tanaka K, Mura T. A theory of fatigue crack initiation at inclusions. Metall Trans A 1982;13A:117–23.
[34] Venkataraman G, Chung YW, Mura T. Acta Metall Mater 1991;39:2621–9.
[35] Chan KS. A microstructure-based fatigue-crack initiation model. Metall Trans A 2003;34A:43–58.
[36] Chan KS. Changes in fatigue life mechanism due to soft grains and hard particles. Int J Fatigue 2009;32:526–34.
[37] Goodman J. Mechanics applied to engineering. 9th ed. New York (NY): Longmans, Green and Co., Inc.; 1930. p. 631–36.
[38] Sendeckyj GP. Constant life diagrams – a historical review. Int J Fatigue 2001;23:347–53.
[39] Fidler TC. A practical treatise on bridge-construction: being a text-book on the design and construction of bridges in iron and steel. London: Charles Griffin and Company; 1877. p. 238–62.
[40] Haigh BP. Experiments on the fatigue of brasses. J Inst Met 1917;18:55–86.
[41] Lindemann J, Wagner L. Mean stress sensitivity in fatigue of α, ($\alpha + \beta$) and β titanium alloys. Mater Sci Eng 1997;A234–236:1118–21.
[42] Lindemann J, Wagner L. Mean stress effect on fatigue strength in titanium alloys. In: Boyer RR, Eylon D, Lutjering G, editors. Fatigue behavior of titanium alloys. Warrendale (PA): TMS; 1999. p. 47–56.
[43] Chesnutt JC, Rhodes CG, Williams JC. Relationship between mechanical properties, microstructure, and fracture topography in $\alpha + \beta$ titanium alloys. In: Fractography-microscopic cracking processes, ASTM STP 600. American Society for Testing and Mater; 1976. p. 99–138.
[44] Lutjering G, Williams JC. Titanium. New York: Springer; 2003. p. 188–89.
[45] Chan KS, Enright MP. Probabilistic micromechanical modeling of fatigue-life variability in an $\alpha + \beta$ Ti alloy. Metall Trans A 2005;36A:2621–31.
[46] Chan KS, Lee Y-D. Effects of deformation-induced constraint on high-cycle fatigue in Ti alloys with a duplex microstructure. Metall Trans A 2008;39A:1665–75.
[47] Lucas JJ. Improvements in the fatigue strength of Ti–6Al–4V forgings. In: Jaffee RI, Burte HM, editors. Titanium, science, and technology, vol. 3. New York (NY): Plenum Press; 1973. p. 2081–95.
[48] Steele RK, McEvily AJ. The effect of mean stress on fatigue behavior of Ti–6Al–4V alloy. In: Williams JC, Belov AF, editors. Titanium and titanium alloys, vol. 1. New York (NY): Plenum Press; 1982. p. 589–600.
[49] Adachi S, Wagner L, Lutjering G. Influence of microstructure and mean stress on fatigue strength of Ti–6Al–4V. In: Lutjering G, Zwicker U, Bunk W, editors. Titanium science and technology. Oberursel, Germany: DGM; 1985. p. 2139–46.
[50] Ivanova SG, Cohen FS, Biederman RR, Sisson Jr RD. Role of microstructure in the mean stress dependence of fatigue strength of Ti–6Al–4V alloy. In: Boyer RR, Eylon D, Lutjering G, editors. Fatigue behavior of titanium alloys. Warrendale (PA): TMS; 1999. p. 39–46.
[51] Ivanova SG, Biederman RR, Sisson Jr RD. Investigation of fatigue crack initiation in Ti–6Al–4V during tensile–tensile fatigue. J Mater Eng Performance 2002;11(2):226–31.
[52] Hanlon T, Kwon Y-N, Suresh S. Grain size effects on the fatigue response of nanocrystalline metals. Scripta Mater 2003;49:675–80.
[53] Hanlon T, Tabachnikova ED, Suresh S. Fatigue behaviors of nanocrystalline metals and alloys. Int J Fatigue 2005;27:1147–58.
[54] Szczepanski CJ, Jha SK, Larsen JM, Jones JW. Microstructural influences on very-high-cycle fatigue-crack initiation in Ti-6246. Metall Mater Trans A 2008;39A:2841–51.
[55] Daeubler MA, Thompson AW. In: Ritchie RO, Lankford J, editors. Small fatigue cracks. Warrendale (PA): The Metallurgical Society; 1986. p. 157–64.
[56] Le Biavant K, Pommier S, Priol C. Local texture and fatigue crack initiation in a Ti–6Al–4V titanium alloy. Fatigue Fract Eng Mater Struct 2002;25:527–45.
[57] Davidson DL, Tryon RG, Oja M, Matthews R, Ravi Chandran KS. Fatigue crack initiation in Waspaloy at 20 °C. Metall Mater Trans A 2007;38A:2214–25.
[58] Bellows RS, Muju S, Nicholas T. Validation of the step test method for generating Haigh diagrams for Ti–6Al–4V. Int J Fatigue 1999;21:687–97.
[59] Bellows R. UDRI final report to AFOSR No. F33615–96-C-5269. Dayton (OH): University of Dayton Research; 2001 [chapter 3, App. 3C].
[60] Bellows R. UDRI final report to AFOSR No. F33615–96-C-5269. Dayton (OH): University of Dayton Research; 2001 [chapter 3, App. 3F].
[61] Atrens A, Hoffelner W, Duerig TW, Allison JE. Subsurface crack initiation in high cycle fatigue in Ti6Al4V and in a typical martensitic stainless steel. Scripta Metall 1983;17:601–6.
[62] Kitagawa H, Takahashi S. Applicability of fracture mechanics to very small cracks or the cracks in the early stage. In: Proceedings of the ICM-2. Metals Park (OH): ASM; 1976. p. 627–31.
[63] Demulsant X, Mendez J. Microstructural effects on small fatigue crack initiation and growth in Ti6Al4V alloys. Fatigue Fract Eng Mater Struct 1995;18(12):1483–97.
[64] Oja M, Ravi Chandran KS, Tryon RG. Orientation imaging microscopy of fatigue crack formation in Waspaloy: crystallographic conditions for crack nucleation. Int J Fatigue 2009;32:551–6.
[65] Sonsino CM, Ziese J. Fatigue strength and applications of cast aluminum alloys with different degree of porosity. Int J Fatigue 1993;15(2):75–84.
[66] Wang QG, Apelian D, Lados DA. Fatigue behavior of A356–T6 aluminum cast alloys. Part I. Effect of casting defects. J Light Met 2001;1(1):73–84.
[67] Lados DA, Apelian D, de Figueredo AM. Fatigue performance of high integrity cast aluminum components. In: Proceedings from the 2nd international

aluminum casting technology symposium, October 7–9, 2002, Columbus, OH. Metals Park (OH): ASM International; 2002. p. 185–96.

[68] Mayer HR, Lipowsky HJ, Papakyriacou M, Rosch R, Stich A, Stanzl-Tschegg S. Application of ultrasound for fatigue testing of lightweight alloys. Fatigue Fract Eng Mater Struct 1999;22:591–9.

[69] Zhu X, Jones JW, Allison JE. Effect of frequency, environment, and temperature on fatigue behavior of E319 cast aluminum alloy: stress-controlled fatigue life response. Metall Mater Trans A 2008;39A:2681–8.

[70] Zhang B, Cockcroft SL, Maijer DM, Zhu JD, Phillion AB. Casting defects in low-pressure die-cast aluminum alloy wheels. JOM 2005(November):36–43.

[71] Chan KS, Jones P, Wang Q. Fatigue crack growth and fracture paths in sand cast B319 and A356 aluminum alloys. Mater Sci Eng A 2003;341:18–34.

[72] Fan J, McDowell DL, Horstemeyer MF, Gall K. Cyclic plasticity at pores and inclusions in cast Al–Si alloys. Eng Fract Mech 2003;70:1281–302.

[73] Fatemi A, Socie DF. A critical plane approach to multiaxial fatigue damage including out-of-plane loading. Fatigue Fract Eng Mater Struct 1988;11(3):149–65.

[74] Hudak Jr SJ, Chell GG, Rennick TS, McClung RC, Davidson DL. A damage tolerance approach to FOD based on the 'worst-case notch' concept. In: Proceedings of the 4th national turbine engine high cycle fatigue conference, Monterey, CA, February 1999.

[75] El Haddad MH, Smith KN, Topper TH. Fatigue crack propagation of short cracks. ASME J Eng Mater Tech 1979;101:42–6.

[76] Frost NE, Marsh KI, Pook LP. Metal fatigue in engineering. New York: John Wiley; 1974.

[77] Sakai T, Takeda M, Shiozawa K, Ochi Y, Nakajima M, Nakamura T, et al. Experimental reconfirmation of characteristic S–N property for high carbon chromium bearing steel in wide life region in rotating bending. J Soc Mater Sci 2000;49:779–85.

[78] Shiozawa K, Lu LT. An effect of shot-peening on super-long-life fatigue behavior in high carbon–chromium bearing steel, JIS SUJ2. In: Proceedings of the 24th symposium fatigue, JSMS; 2000. p. 207–10.

[79] Tanaka K, Akiniwa Y. Fatigue crack propagation behavior derived from S–N data in very high cycle regime. Fatigue Fract Eng Mater Struct 2002;25:775–84.

[80] Bathia C. There is no infinite fatigue life in metallic materials. Fatigue Fract Eng Mater Struct 1999;22:559–65.

[81] Wang QY, Berard JY, Rathery S, Bathia C. High-cycle fatigue crack initiation and propagation behavior of high-strength spring steel wires. Fatigue Fract Eng Mater Struct 1999;22:673–7.

[82] Wang QY, Berard JY, Dubarre A, Baudry G, Rathery S, Bathias C. Gigacycle fatigue of ferrous alloys. Fatigue Fract Eng Mater Struct 1999;22:667–72.

[83] Wang QY, Bathias C, Kawagoishi N, Chen Q. Effect of inclusion on subsurface crack initiation and gigacycle fatigue strength. Int J Fatigue 2002;24:1269–74.

[84] Hyzak JM, Bernstein IM. The effect of defects on the fatigue crack initiation process in two P/M superalloys: Part I. Fatigue origins. Metall Trans A 1982;13A:33–43.

[85] Chang DR, Krueger D, Sprague RA. Superalloy powder processing, properties and turbine disk applications. In: Superalloys 1984; 1984. p. 245–73.

[86] Huron ES, Roth PG. The influence of inclusion on low cycle fatigue life in a P/M nickel-base disk superalloy. In: Kissinger RD, Deye DJ, Anton DL, Cetel AD, Nathal MV, Pollock TM, Woodford DA, editors. Superalloys 1996. The Minerals, Metals, and Materials Society; 1996. p. 359–68.

[87] Jablonski DA. The effect of ceramic inclusions on the low cycle fatigue life of low carbon astrology subjected to hot isostatic pressing. Mater Sci Eng 1981;48:189–98.

[88] Alexandre F, Deyber S, Pineau A. Modelling the optimum grain size on the low cycle fatigue life of a Ni based superalloy in the presence of two possible crack initiation sites. Scripta Mater 2004;50:25–30.

[89] Kunz L, Lukas P, Konecna R. High-cycle fatigue of Ni-base superalloy Inconel 713LC. Int J Fatigue 2009;32:908–13.

[90] Bathias C, Paris PC. Gigacycle fatigue of metallic aircraft components. Int J Fatigue 2009;32:894–7.

[91] Gabb TP, Gayda J, Telesman J, Kantzos PT. Thermal and mechanical property characterization of the advanced disk alloy LSHR. NASA/TM – 2005-213645, June 2005.

[92] Jha SK, Caton MJ, Larsen JM. A new paradigm of fatigue variability behavior and implications for life prediction. Mater Sci Eng A 2007;468–470:23–32.

[93] Jha SK, Caton MJ, Larsen JM. Mean vs. life-limiting fatigue behavior of a nickel-based superalloy. In: Reed RC et al., editors. Superalloy 2008. Warrendale (PA): TMS; 2008. p. 565–72.

[94] National Transportation Safety Board. Aircraft Accident Report – United Airlines Flight 232 McDonnell Douglas DC-10-10 Sioux Gateway Airport, Sioux City, Iowa, July 19, 1989. Washington, DC: National Transportation Safety Board, NTSB/AAR-90/06; 1990.

[95] McDowell DL, Gall K, Horstemeyer MF, Fan J. Microstructure-based fatigue modeling of cast A356–T6 alloy. Eng Fract Mech 2003;70:49–80.

[96] Prasannavenkatatesan R, Zhang J, McDowell DL, Olson GB, Jou H-J. 3D modeling of subsurface fatigue crack nucleation potency of primary inclusions in heat treated and shot peened martensitic gear steels. Int J Fatigue 2009;31:1176–89.

[97] Brooksbank D, Andrews KW. Tessellated stresses associated with some inclusions in steel. J Iron Steel Inst 1969:474–83.

[98] Laz PJ, Chan KS, McClung RC, Leverant GR. Effects of CTE-induced residual stresses around hard alpha particles on fatigue crack growth in Ti–6Al–4V. Fatigue Fract Eng Mater Struct 2003;26(12):1145–57.

[99] Dieter Jr GE. Mechanical metallurgy. New York (NY): McGraw-Hill; 1961. p. 323–26.

[100] Manonukul A, Dunne FP. High- and low-cycle fatigue crack initiation using polycrystal plasticity. Proc Roy Soc London A 2004;460:1881–903.

[101] Shenoy M, Tjiptowidjojo Y, McDowell D. Microstructure-sensitive modeling of polycrystalline IN 00. Int J Plast 2008;24:1694–730.

[102] Tjiptowidjojo Y, Przybyla C, Shenoy M, McDowell D. Microstructure-sensitive notch root analysis for dwell fatigue in Ni-base superalloys. Int J Fatigue 2009;31:515–25.

[103] Shenoy M, Zhang J, McDowell D. Estimating fatigue sensitivity to polycrystalline Ni-base superalloy microstructures using a computational approach. Fatigue Fract Eng Mater Struct 2007;30:889–904.

[104] National Transportation Safety Board. Aircraft Accident Report – Uncontained Engine Failure, Delta Airlines Flight 1288 McDonnell Douglas MD-88, N927DA, Pensacola, Florida, July 6, 1996. Washington, DC: National Transportation Safety Board, NTSB/AAR-98/01; 1998.

[105] US Air Force. <http://www.af.mil/news/story.asp?storyID=123081718>.

[106] Arola D, Williams CL. Estimating the fatigue stress concentration factor of machined surfaces. Int J Fatigue 2002;24:923–30.

[107] Yuri T, Ono Y, Ogata T. Effect of surface roughness and notch on fatigue properties for Ti–5Al–2.5Sn ELI alloy at cryogenic temperatures. Sci Technol Adv Mater 2003;4:291–9.

[108] As SK, Skallerud B, Tveiten BW, Holme B. Fatigue life prediction of machined components using finite element analysis of surface topography. Int J Fatigue 2005;27:1590–6.

[109] Suraratchai M, Limido J, Mabru C, Chieragatti R. Modelling the influence of machined surfaces on the fatigue life of aluminum alloy. Int J Fatigue 2008;30:2119–26.

[110] Konig GW. Life enhancement of aero engine components by shot peening: opportunities and risks. In: Wagner L, editor. Shot peening. Weinheim, Germany: Wiley-VCH; 2003. p. 13–23.

[111] Prevey PS. The effect of low plasticity burnishing (LPB) on the HCF performance and FOD resistance of Ti–6Al–4V. In: Proceedings of 6th national turbine engine high cycle fatigue (HCF) conference, March 5–8, 2001, Jacksonville, FL.

[112] Prevey PS, Jayaraman N, Shepard MJ. Improved HCF performance and FOD tolerance of surface treated Ti–6–2–4–6 compressor blades. In: Proceedings of the 9th national turbine engine high cycle fatigue conference, 2004, Pinehurst, NC.

[113] Wareing J. Vaughan HG. Metal Sciences 1979;13:1–8.

[114] Buckner BD, Markov V, Lai L, Earthman JC. Opt Eng 2008;47(5):054402.

[115] Brinckmann S, Van der Giessen E. A fatigue crack initiation model incorporating discrete dislocation plasticity and surface roughness. Int J Fract 2007;148:155–67.

[116] Davidson DL, Lankford J. Fatigue crack growth in metals and alloys: mechanisms and micromechanics. Int Mater Rev 1992;37:45.